Harnessing topological modes of light with digital holography

by

Argha Mondal

A dissertation submitted in partial fulfillment

of the requirements for the degree of

Doctor of Philosophy

Department of Physics

New York University

January, 2020

David G. Grier

Dedication

To my family.

Acknowledgments

It has been a great pleasure to be a part of the Center for Soft Matter Research at the Department of Physics at New York University. I would like to take this opportunity to express my gratitude to everyone who has assisted me during my PhD time. This thesis would not have been possible to be completed without their help.

First and foremost, I would like to acknowledge Professor David G. Grier, my thesis advisor. David has been an incredible and patient mentor throughout my graduate career. He has taught me, both consciously and unconsciously, how good experimental physics is done. David's creativity and deep insight arising from his open mind to nature and human was contagious and motivational for me, even during tough times in the Ph.D. pursuit. His encouragement and unfailing optimism have driven me to move on steadfastly. The kindness, energy, enthusiasm, and humor he has ushered have filled the lab with warm and inspirational atmosphere all the time. Thank you especially for the painstaking editing of this thesis! I am grateful for the great work environment that you created with your positive attitude.

I am grateful to my thesis committee, Paul Chaikin, Andrew Wray, Marc

Gershaw , who supported me through the thesis process. Thank you for your questions, motivation and feedback. Special thanks to Alexander Grosberg who taught me soft matter physics.

Grierlings (members of the Grier group) are some of the most intellectual and inspiring people I have met, who will be difficult to find elsewhere. I am thankful for the overlap in my tenure I have shared with Henrique, Daniel, Chen, Mark, Aaron, Jordan, Mohammed, and Lauren. Thanks to Henrique Moyses for kick-starting my research career and teaching me all the experimental techniques as a newcomer. Thanks to Chen Wang for his help right from the beginning of my Ph.D. till today with pretty much everything including precious suggestions on my research, and job hunting. Thanks to Mark Hannel for being a great academic example everyday and coaching me all the time. I appreciate all those discussions about statistical physics, digital holography, machine learning and countless banter. Thank you for your honest feedback which helped me grow. I am grateful for the collaboration with Aaron Yevick. Without you and David Ruffner the research in this thesis would not have started.

I would like to thank everyone else in the Physics Department, especially at CSMR who made all of the paperwork look so easy. Thank you Jessica Ong and Evette Ma for your assistance. Thanks to Mark Ofitserov for making things work in the lab. Thanks also to Andrew Hollingsworth for answering all of my questions about the lab and even about basic chemistry.

I must thank my classmates and office mates who had my back throughout our time here. My time at NYU was made enjoyable in large part due to the many friends and groups that became a part of my life. I am grateful for time spent with roommates and friends, for my backpacking buddies and our memorable trips into the mountains, and oceans. Special thanks to Yishuai Xu for all those playoffs. Maybe one day we will master our backhand in tennis and also serve like Federer at court. Thanks to Daniel, Mark, Melissa, Lauren, Jordan for being the best neighbors everyday.

And finally, I would also like to say a heartfelt thank you to my parents for always believing in me and encouraging me to follow my dreams. Thanks also to Bratati whose support during the entirety of this Ph.D. is so appreciated. This dissertation would not have been possible without their warm love, continued patience, and endless support. Thank you.

Abstract

A beam of light is traveling electromagnetic wave and that has the ability to transfer linear and angular momentum to an illuminated object. This ability can be used to capture and guide small particles along chosen trajectories. One special scenario involves trapping and pulling objects towards the source of the beam of light over a long range, opposite to the direction of propagation. A wave that pulls has long been known in science fiction literature as a "tractor beam". Quite remarkably light waves that act as tractor beam have been demonstrated experimentally. To generate such a force field the mode of light, which is known as a "tractor beam", is a superposition of non-diffracting Bessel beams with special chosen characteristics. Generating such a mode of light involves designing the electromagnetic wave that exerts the desired force field by creating an optical system to project that mode. This thesis addresses both of these challenges and explores the nature of the "accelerating" mode of light that act as a tractor beam.

The goal of this thesis is to achieve long range optical micromanipulation of colloidal particles. After a brief description to the field in Chapter 1, this thesis presents in Chapter 2 the formalism used to describe the propagation and diffraction of electromagnetic waves, so called topological modes of light. 3 introduces

the holographic creation of propagation invariant modes of light and discusses their applications. In Chapter 4 we introduce a new experimental technique called "Intermediate Plane Holography" which can extend the range of any non-diffracting mode of light. We demonstrate this technique through the first experimental realization of meter-class tractor beams. Finally, we use intermediate plane holography to create modes of light that appear, in themselves to be sccelerating and therefore to violate Ehrenfest's theorem. Chapter 5 introduces and resolves this paradox.

Contents

List of Figures

Chapter 1

Introduction

1.1 Why is this Problem Relevant?

From Maxwell's theory it is known that an electromagnetic wave or optical field carries both momentum and energy. Momentum can be further decomposed into linear and angular momentum, where angular momentum has two components: the spatial structure gives rise to orbital angular momentum [1] and its polarization is associated with the spin angular momentum. Therefore any interaction between the optical field and matter will give rise to momentum transfer hence a force acting on the illuminated body. A simple plane electromagnetic wave exerts uniform radiation pressure that pushes any object downstream, away from the source. Multiple plane waves can be superposed in a way that generates attractive forces that pull an object upstream towards the source. Such a superposition of plane waves was first discovered by Arthur Ashkin and his co-workers at Bell Labs in 1986 [2], and is known as optical tweezers. Since this discovery, optical manipulation has become an active topic of research, where complex optical fields are generated using various means and serve purposes ranging from non-invasive manipulation of biological samples to fundamental studies in statistical phywics XXXXX REF XXXXX.

An interest in deep space exploration has inspired the desire to answer the question: what kind of useful force can light exert on an object at a great distance? Similarly the commercial need for faster optical communication systems has inspired research in to the practical limits on the propagation distance of structured optical fields. In this thesis we explore options to make "long-range tractor beams" into a reality and understand their properties.

Understanding the local properties of a beam of light is the starting point for studying the evolution of an optical field and the forces generated by it. The energy flux of a plane wave can be calculated using the Poynting vector, which also provide insights to the direction of the radiation pressure. Radiation pressure can be counteracted by forces engineered by the intensity gradient which ultimately can form a trap for small particles. Small dielectric particles for example feel an attractive force towards the point of maximum intensity.

The limitation of a point optical trap created using strongly focused laser beam with a high intensity gradient is its range. The distance over which the intensity gradient force can overcome the radiation force goes only up to the order of $1\,\mu$m.This limitation revise the question if whether any mode of light can manipulate objects over such a long ranges. The ideal optical mode for long range manipulation would be propagation invariant and would create a net negative force field along its entire length when it interacts with an object. Previously, exotic modes were created which are spiraling around their axis were shown to act as a tractor beam [3]. But such tractor beams were realized over $\sim 100\mu$m only. Here we present intermediate plane holography a new experimental technique for creating such tractor beams with increased power efficiency and larger propagation invariant range.

Due to the homology of paraxial wave equation with Schrodinger's equation the spatial structure of a propagating beam of light is analogous to the temporal evolution of a quantum mechanical wave packet. Therefore we can use optics to understand complex quantum mechanical states. A spiraling beam of light is a superposition of multiple Bessel beam with non-zero angular momentum. A similar wave function arises inside a infinite cylindrical wall in quantum mechanics. In this thesis we have studied the propagation of a spiral beam to understand the evolution of a Bessel like quantum state under a force free condition, which is a class of accelerating beam in the same sense as reported by Berry and Balazs [4].

1.2 Organization

This thesis is organized in the following manner:

Chapter 2 starts with a brief historical motivation behind understanding the properties of light followed by the basic formalism for describing it in terms of electric and magnetic field. We introduce the generalized version of Maxwell's equations and arrive at the general solutions of electric and magnetic field which are the solution of wave equations. In order to maintain consistency we introduce the parameters used in our experiments and use them to describe the propagation of electric field.

Using the fundamental description of light, in Chapter 3, we describe different types of topological modes of light generated using digital holographic technique.

Chapter 4 introduces a new technique called "Intermediate Plane Holography (IPH)" for structuring laser beams with computer-generated holograms. IPH can dramatically improve both diffraction efficiency and mode purity. We illustrate these capabilities by projecting Bessel beams, which constitute the natural basis for propagation-invariant modes [5, 6].

Chapter 5 presents a new class of accelerating beam in two dimensions. Here we demonstrate that a shape-preserving wave packets that rotate at constant angular speed around the center of the box follows Ehrenfest's theorem. The apparent violation of Ehrenfest's theorem is resolved by considering the force exerted on the particle's wave packet by the enclosing wall.

Finally, Chapter 6 shows possible pathways for extending research in this field and its applications. (Yet to be done!!)

Chapter 2

Fundamentals of Light

2.1 History of Optics

The systematic story of light dates back at least to the ancient Greek Philosophers [7], who sought to understand the nature of light and its role in visual perception. Three school of thought originated from those studies: (1) The Pythagorans inferred that something emitted by the eye interacted with the object in front to create an image. (2) Democritus hypothesized exactly the opposite; that light is something the objects create that carries information about the object's shape and color, which interacts with the human eye. Followers of (3) Empedocles believed light to be a combined process of the previous two ideas. Thus philosophical investigation turned quantitative with Euclid's introduction of geometric optics in 300 B.C.[8], specifically with his discovery of the law of reflection. The ensuing two millennium of observations and the theorizing about the nature of light were distilled in the eighteen century into two competing theories: the corpuscular the-

Fig. 2.1: Three of the most popular school of thought about the properties of light in the age of Greek philosophers: Pythagoras (left) conjectured that eyes interacted with an object by emitting something. Source: FixQuotes.com [9]. Democritus's (middle) view was the opposite; the eyes receive information about the object through something which is emitted by the item. Source: Atomic Model Timeline [10]. And Empedocles (right) believed both the eyes and the object emits information in some form in order for it to be perceived by humans. Source: History-biography.com [11]. XXXX [Change image ref]

ory of light proposed by Newton in his Optics XXXXX [Find ref] (1704) and the wave theory developed by Huygens, XXXXX [Find ref] and others. It took more than 1500 years after that when Huygens (1690) considered the wave like nature of light. Another two centuries passed before this dichotomy was resolved with the quantitative theory of light. The present thesis takes light as a wave and adopts the analytical solution of wave optics pioneered by Fresnel in 1819. Fresnel paved the way for a solid wave theory of light by conducting several experiments which confirmed that light propagates as a sum of Huygens wave.

2.2 Light is Electromagnetic Waves

Fifty years after Fresnel first formulated wave optics, Maxwell provided theoretical foundation for the wave theory of light through his theory for electromagnetism first reported in 1861. Maxwell synthesized the preceding century

of the now famous Maxwell's Equations which can be found in his 1861 paper [12]. These equations :

$$\nabla \cdot \boldsymbol{E} = \frac{\rho}{\epsilon_0} \quad , \quad \text{(Coulomb)} \tag{2.1a}$$

$$\nabla \cdot \boldsymbol{B} = 0 \quad , \quad \text{(Gauss)} \tag{2.1b}$$

$$\nabla \times \boldsymbol{E} = -\frac{\partial \boldsymbol{B}}{\partial t} \quad , \quad \text{(Faraday)} \tag{2.1c}$$

$$\nabla \times \boldsymbol{B} = \mu_0 \boldsymbol{J} + \mu_0 \epsilon_0 \frac{\partial \boldsymbol{E}}{\partial t} \quad , \quad \text{(Ampère)} \tag{2.1d}$$

These four equations summarize how the time varying fields $\boldsymbol{E}(\boldsymbol{r}, t)$ and $\boldsymbol{H}(\boldsymbol{r}, t)$ are related to electric charge density $\rho(\boldsymbol{r}, t)$ and the electric current density $\boldsymbol{J}(\boldsymbol{r}, t)$. Equation (2.1a), also known as the Gauss' Law, tells us how charge density creates electric field. Equation (2.1b) states the experimental fact that magnetic monopoles do not seem to exist, which requires that divergence of the magnetic field $\boldsymbol{H}(\boldsymbol{r}, t)$ must vanish. Equation (2.1d) also known as Faraday's Law that shows current can be induced with in a loop or wire if a changing magnetic field slices through it. The fourth of the Maxwell's Equations describes how electric current give rise to magnetic fields.This typically is credited to Ampère's although Maxwell himself incorporated the coupling between $\boldsymbol{E}(\boldsymbol{r}, t)$ and $\boldsymbol{H}(\boldsymbol{r}, t)$ to obtain a symmetric set of equations. In vacuum $\rho(\boldsymbol{r}, t) = 0$ and $\boldsymbol{J}(\boldsymbol{r}, t) = 0$ so that Maxwell's Equations simplify to :

$$\nabla \cdot \boldsymbol{E} = 0 \quad , \quad \nabla \times \boldsymbol{E} = -\frac{\partial \boldsymbol{B}}{\partial t} \tag{2.2a}$$

$$\nabla \cdot \boldsymbol{B} = 0 \quad , \quad \nabla \times \boldsymbol{B} = \mu_0 \epsilon_0 \frac{\partial \boldsymbol{E}}{\partial t} \tag{2.2b}$$

Taking the curl of Eq. (2.2a) and Eq. (2.2b) we obtain the wave equations for the electric and magnetic fields:

$$\left(\nabla^2 + \frac{1}{c^2} \frac{\partial^2}{\partial t^2} \right) \boldsymbol{E} = 0 \quad , \tag{2.3a}$$

$$\left(\nabla^2 + \frac{1}{c^2} \frac{\partial^2}{\partial t^2} \right) \boldsymbol{B} = 0 \quad , \tag{2.3b}$$

where the constant c is defined as:

$$c = \frac{1}{\sqrt{\mu_0 \epsilon_0}} \quad , \tag{2.4}$$

which is same as the speed of light. In 1865 Maxwell noted that c is consistent with the speed of light as suggested in this thesis that light is an electromagnetic wave [13]. The same wave equations also predicted the existence of electromagnetic wave with frequencies outside the range of visual perception. Later between 1886 and 1889 Hertz conducted several experiments to prove Maxwell's prediction. In his seminal paper: "On Electromagnetic Effects Produced by Electrical Disturbances in Insulators", Hertz showed that electromagnetic waves traveling at the speed of light [14].

2.3 Solution of Wave Equations

The general solutions to Eq. (2.3a) and Eq. (2.3b),

$$\boldsymbol{E}(\boldsymbol{r},t) = E_0 \exp\left(i\boldsymbol{k}\cdot\boldsymbol{r} - i\omega t\right)\boldsymbol{\varepsilon} \quad \text{and} \tag{2.5a}$$

$$\boldsymbol{B}(\boldsymbol{r},t) = \frac{E_0}{c} \exp\left(i\boldsymbol{k}\cdot\boldsymbol{r} - i\omega t\right)\hat{k}\times\boldsymbol{\varepsilon} \tag{2.5b}$$

represent monochromatic plane waves [15], where $\boldsymbol{k}$ is the wave vector that tells us the direction of propagation of the wave and $\boldsymbol{\varepsilon}$ is the axis of polarization. The wave number $k = |\boldsymbol{k}|$ is connected to c, the speed of light, through the dispersion relation: $k = \omega/c$ and the wavelength can be calculated from $\lambda = 2\pi/k$. Both electric (Eq. (2.5a)) and magnetic (Eq. (2.5b)) fields are represented as a complex-valued functions because it is convenient for calculation. $\Re\left\{\boldsymbol{E}\left(\boldsymbol{r},t\right)\right\}$ and $\Re\left\{\boldsymbol{H}(\boldsymbol{r},t)\right\}$ are the real part of $\boldsymbol{E}\left(\boldsymbol{r},t\right)$, and $\boldsymbol{H}(\boldsymbol{r},t)$ respectively and they correspond to the actual electric and magnetic field. The work described in this thesis is carried out with linearly polarized light, and we all adopt the convention $\hat{\epsilon} = \hat{x}$, due to the nature of our experimental setup, from here on.

2.4 Experimental Parameters

In Cartesian coordinates the light field can be described by six complex valued functions, two for each coordinate axis. The electric field of a monochromatic beam of light in Cartesian coordinate can be described as:

$$\boldsymbol{E}(\boldsymbol{r},t) = \sum_{j=1}^{3} E_j\left(\boldsymbol{r}\right)\exp\left(-i\omega t\right)\boldsymbol{\varepsilon_j}(\boldsymbol{r}) \tag{2.6}$$

where $E_j(\boldsymbol{r})$ is the complex scalar field and ω is the frequency of the light. As described in 2.3 we only work with linearly polarized light. $E_j(\boldsymbol{r})$ is a solution of the Helmholtz Equation [16]:

$$\left(\nabla^2 + k^2\right)E = 0 \tag{2.7}$$

and in the paraxial limit of the Helmholtz Equation $E_j(\boldsymbol{r})$ can be expressed as:

$$E_j\left(\boldsymbol{r}\right) = u_j\left(\boldsymbol{r}\right)e^{i\phi_j(\boldsymbol{r})} \quad , \tag{2.8}$$

where $u_j(\boldsymbol{r})$ is the amplitude and $\phi(\boldsymbol{r})$ is the phase of the scalar field.

2.5 Diffraction of Light

The first quantitative study of the deviation of light from its rectilinear propagation [17], is a phenomenon known as "diffraction", was reported by Francesco Grimaldi [18] in 1665. A great victory of the wave theory of light is its ability to account naturally for diffraction. This description underlies the approach adopted in this thesis to describe the holographic video microscopy and holographical optical trapping. To understand digital holographic microscopy [19] it is essential to understand the limitations imposed by diffraction.

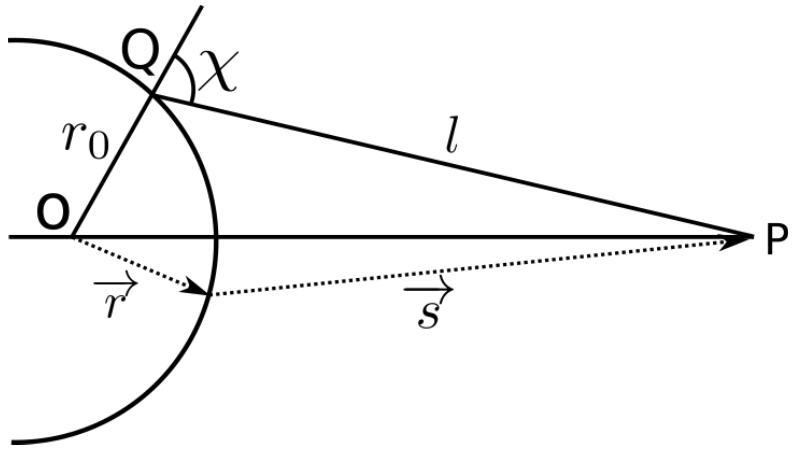

Fig. 2.2: According to Huygens-Fresnel principle a sample point **Q** is considered as a secondary source which emits a spherical wavefront. The electric field at point **P** is a superposition of all secondary wavefronts created on the surface of the parent wavefront with center at **O**.

2.5.1 Rayleigh-Sommerfeld Diffraction Theory

According to Huygens principle every point on a wavefront of a wave can be considered to be a secondary source which creates a spherical wavefront. Fresnel proposed that such secondary wavefronts recreate the wavefronts of the primary wave by interfering with each other, is known as the "Huygens - Fresnel Principle". Using the geometry presented in the Fig.2.2 , the electric field at point "**P**" due to the secondary wave generated a small area dS at point "**Q**" can be written as:

$$dE(\boldsymbol{P}) = K(\chi)\frac{u_0 e^{ik\cdot r_0}}{r_0}\frac{e^{i\boldsymbol{k}\cdot\boldsymbol{\ell}}}{\ell}d\boldsymbol{S} \quad , \tag{2.9}$$

where r_0 is the radius of the parent spherical wavefront originated from point "**O**" and ℓ is the distance between point "**Q**" and "**P**". $K(\chi)$ is the inclination factor which is maximum (1) when the propagation direction "**OQ**" aligns with "**OP**".

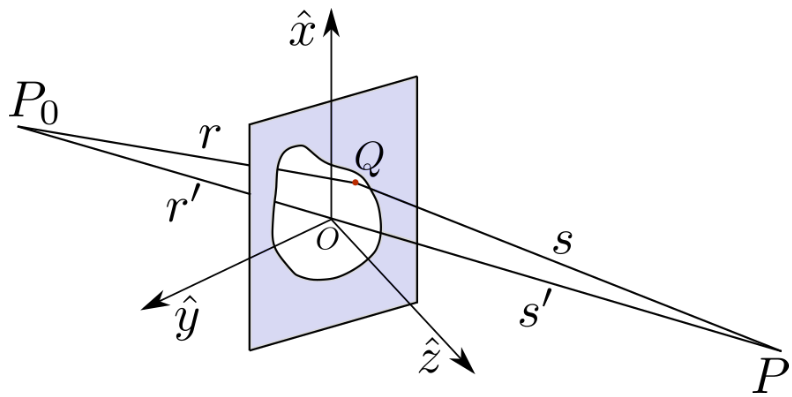

Fig. 2.3: Fresnel-Kirchoff Diffraction formula describes the electric field at point **P** due to a point source placed at $\mathbf{P_0}$ and an aperture placed in between.

Therefore the total field at "**P**" will be:

$$E(\boldsymbol{P}) = \frac{u_0 e^{ikr_0}}{r_0} \int\int_S \frac{e^{i\boldsymbol{ks}}}{s} K(\chi) d\boldsymbol{S} \quad . \tag{2.10}$$

Kirchoff [20] showed that Huygens-Fresnel principle is an approximation of the now well known "Fresnel-Kirchoff Diffraction Formula":

$$E(\boldsymbol{P}) = -\frac{iu_0}{2\lambda} \int\int_S \frac{e^{ik(r+s)}}{rs} \left[\cos(\boldsymbol{n}, \boldsymbol{r}) - \cos(\boldsymbol{n}, \boldsymbol{s})\right] d\boldsymbol{S} \quad , \tag{2.11}$$

which describes the electric field at **P** due to diffraction of light originated at $\mathbf{P_0}$ through a planar aperture as depicted in Fig. 2.3. The boundary conditions imposed on both the field and its normal derivative in order to obtain the Fresnel-Kirchhoff diffraction formula are known to be mathematically inconsistent [21–23]. The diffraction formula shows strong deviation from the physical solution when the observation point is close to the diffracting screen. It also yields an incorrect intensity pattern for Poisson's spot created by diffraction from an annular aperture. Sommerfeld corrected these inconsistencies by choosing an alternative Green's function and removing the boundary condition on the normal derivative of the field. His solution:

$$E(\boldsymbol{P}) = -\frac{iu_0}{\lambda}\int\int_S \frac{e^{i\boldsymbol{k}(\boldsymbol{r}+\boldsymbol{s})}}{rs}\cos(\boldsymbol{n},\boldsymbol{s})d\boldsymbol{S} \quad , \tag{2.12}$$

is known as the "Rayleigh-Sommerfeld Diffraction Formula".

2.5.2 Fresnel and Fraunhofer Diffraction

Equation (2.12) can be rewritten in terms of the field in the aperture as:

$$E(\boldsymbol{P}) = \frac{1}{i\lambda}\int\int_S E(\boldsymbol{Q})\frac{e^{i\boldsymbol{k}\boldsymbol{s}}}{s}\cos(\theta)d\boldsymbol{S} \quad , \tag{2.13}$$

where $E(\boldsymbol{Q})$ is the field at $\mathbf{Q}$ on the aperture and θ is $\cos(\boldsymbol{n},\boldsymbol{s})$, the angle between the normal to the aperture and the vector $\boldsymbol{s}$. Assuming Cartesian coordinates to these points,

$$P_0 \equiv (x_0, y_0, z_0) \quad , \tag{2.14a}$$

$$P \equiv (x, y, z) \quad , \tag{2.14b}$$

$$Q \equiv (\xi, \eta) \tag{2.14c}$$

yields $\cos\theta = \frac{z}{s}$ and the Eq. (2.13) simplifies to:

$$E\left(x, y\right) = \frac{z}{i\lambda}\int\int_S E(\xi,\eta)\frac{e^{i\boldsymbol{k}\boldsymbol{s}}}{s^2}d\xi d\eta \quad , \tag{2.15}$$

where:

$$s = \sqrt{z^2 + (x-\xi)^2 + (y-\eta)^2} \quad . \tag{2.16}$$

The Fresnel approximation:

$$s \approx z\left[1 + \frac{1}{2}\left(\frac{x-\xi}{z}\right)^2 + \frac{1}{2}\left(\frac{y-\eta}{z}\right)^2\right] \tag{2.17}$$

further simplifies Eq. (2.15) and we get:

$$\begin{aligned} E(x,y) = \frac{e^{ikz}}{i\lambda z} e^{i\frac{k}{2z}(x^2+y^2)} \int\int_S & E(\xi,\eta)\, e^{i\frac{k}{2z}(\xi^2+\eta^2)} \\ & \times e^{-i\frac{k}{2z}(x\xi+y\eta)} d\xi d\eta \quad , \end{aligned} \tag{2.18}$$

which is valid in the near field of the aperture. In the far-field the Fraunhofer approximation [16]:

$$z \gg \frac{k(\xi^2+\eta^2)}{2} \tag{2.19}$$

simplifies Eq. (2.18) even further to:

$$E(x,y) = \frac{e^{ikz}}{i\lambda z} e^{i\frac{k}{2z}(x^2+y^2)} \int\int_S E(\xi,\eta)\, e^{-i\frac{k}{2z}(x\xi+y\eta)} d\xi d\eta \quad , \tag{2.20}$$

which is same as the Fourier transform of the field in the aperture.

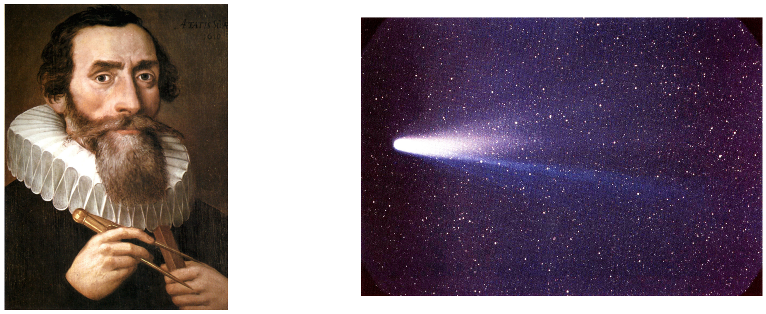

Fig. 2.4: German mathematician and astronomer Johannes Kepler (left) conjectured the radiation pressure of sunlight could explain why comet tails always point away from the sun including the Halley's comet's (right) tail. Source: Wikipedia [24, 25].

2.6 Optical Forces

> "It is probable that a much greater energy of radiation might be obtained by means of concentrated rays from an electric lamp. Such rays falling on a thin metallic disc, delicately suspended in a vacuum, might perhaps produce an observable mechanical effect"
>
> *J C Maxwell, 1873*

The first proposal that light might exert forces was made by Kepler in 1619, when he suggested the tail of Halley's comet might be created by the radiation pressure of sunlight. Two and a half centuries later Maxwell used his theory of electromagnetism to demonstrate that electromagnetic waves carry momentum and that this momentum can be transferred to illuminated objects as radiation pressure while it interacts with the object. This momentum transfer can happen either via reflection/scattering or absorption.

In the past fifty years there has been a significant increase in the interest of understanding forces exerted by an electromagnetic wave interacting with small objects. Arthur Ashkin first pointed out in 1970 that optical forces could provide convenient ways to control the dynamics of small objects and that this would have major applications inatomic physics, biology and nonlinear physics. Light electric field and magnetic field exert forces on small neutral objects by inducing time varying chharge multipoles in them and then exerting forces and torques on the induced multipoles [Find ref] [15, 26–28]. For particles that are much smaller than the wavelength of light the Lorentz force is dominated by dipole contributions. The induced dipole moment experience a force in gradients of the electric field $(\boldsymbol{p} \cdot \boldsymbol{\nabla})\boldsymbol{E}$. The time-varying dipole moment acts like a current that couples to the magnetic field, $\dot{\boldsymbol{p}} \times \boldsymbol{B}$. The resulting dipole order force has the time averaged form [27]

$$\boldsymbol{F_e} = \frac{1}{2}\Re\{(\boldsymbol{p} \cdot \boldsymbol{\nabla})\boldsymbol{E}^\star + \frac{1}{c}\dot{\boldsymbol{p}} \times \boldsymbol{B}^\star\} \tag{2.21}$$

The induced dipole is proportional to the local electric field, $\hat{\boldsymbol{p}} = \alpha_e \hat{\boldsymbol{E}}$, where α_e is the particle's electric dipole polarizability. In 2000, Chaumet and Vesperinas [26] ahowed that Eq. (2.21) could be rewritten in the compact and evocative form:

$$\boldsymbol{F_e} = \frac{1}{2}\Re\{\alpha_e E_j \partial_i E_j^\star\} \quad , \tag{2.22}$$

This form is useful for developing a practical framework for controlling optical forces. The optical force is parametrized by the object's polarizability, which depends on its size,shape and chemical composition. α_e is complex valued and can written as $\alpha_e = \alpha_e' + i\alpha_e''$, where α_e' and α_e'' are the real and imaginary part [15] respectively. The imaginary part of the polarizability accounts for absorption and radiative losses. For the special case of a sphere of radius a_p and refractive index n_p in a medium with refractive index n_m the electric polarizability is given by the Clausius-Mosotti-Draine relationship [29]:

$$\alpha_e = \frac{4\pi\epsilon_0 n_m^2 K a_p^3}{1 - i\frac{2}{3}Kk^3 a_p^3} \quad \text{, where} \quad K = \frac{n_p^2 - n_m^2}{n_p^2 + 2n_m^2}. \tag{2.23}$$

Here ϵ_0 is the permittivity of space and k is the wave number of the light. Equation. (2.22) and Eq. (2.23) specify what force can be expected from a specified electric light field. They are less useful for designing waves to exert derived forces. A more interpretable expression can be obtained by replacing the electric fields in Eq. (2.21) with Eq. (2.8) which yields:

$$\boldsymbol{F_e}(\boldsymbol{r}) = \frac{\omega^2}{4}\alpha_e' \sum_{j=0}^{2} \nabla u_j^2(\boldsymbol{r}) + \frac{\omega^2}{2}\alpha_e'' \sum_{j=0}^{2} \nabla u_j^2 \phi_j(\boldsymbol{r}) \tag{2.24}$$

The first term in Eq. (2.24) is proportional to the gradient of the light intensity. It is manifestly conservative and tends to draw dielectric particles ($\alpha_e' > 0$) toward intensity maxima. This intensity gradient force allows focused beams if light to trap small objects in three dimensions, thereby acting as "optical tweezers" [30]. The second term in Eq. (2.24) is directed by gradients of the phase and describes a non-conservative force that identify with the radiative pressure.

Chapter 3

Holographic Creation of Topological Modes of Light

3.1 Topological Modes of Light

> "Topology is the mathematical study of the properties that are preserved through deformations, twistings, and stretchings of objects [31]"
>
> *Wolfram MathWorld, "Topology"*

It is the study of complex multidimensional curves and surfaces. By "Topological Photonics" [32, 33] majority of the researchers in the field of material science and hard condensed matter physics fundamentally think of discovering a new class of photonic-structure [34] that are able to transport light around sharp angles without back scattering. With these wave-guides scientists are able to realize exotic edge states with interesting properties that are found in topological insulators [35, 36]. While this field of research has applications in multiple areas [37] including photonic crystals, waveguides, metamaterials, cavities, optomechanics, silicon photonics, and circuit QED, we will digress from the generic meaning of the term. In this thesis we consider the study of global and local shape of the wavefront of a light field as "Topological Photonics".

Many applications of structured light field require a mode of light with specified intensity distribution in a certain plane. The ability to focus a beam of light in a specific shape in space is useful for fields ranging from cryptography [38, 39] to biology [40, 41], and neuroscience [XXXX ADD NEURO REFERENCE]. Therefore, understanding the topology of a wavefront is necessary as it determines the evolution of the electric field in space.

Non-trivial wavefronts often feature phase singularities [42]. One of the simplest examples of a topological defect in a mode of light is a screw dislocation [42] in the wavefront. This gives rise to a helical wavefront where the phase changes by $2m\pi$ upon one revolution around the axis of propagation. Here m is an integer that describes the pitch of the wavefronts' curvature. Imposing a helical pitch on the phase introduces a helical mode's intensity distribution. Helical modes are dark [42, 45] on axis because all phase angles appear along the axis of the associated screw dislocation causing destructive interference. The beam's intensity is redistributed to a ring whose radius depends on the winding number m. Changing the topological charge therefore changes the intensity distribution of a helical mode of light. An ordinary TEM_{00} laser mode can be converted into a helical mode with spiral phase plate that imposes the required phase ramp in a particular plane. A spiral plate [46] also can convert a helical mode into another. Apart

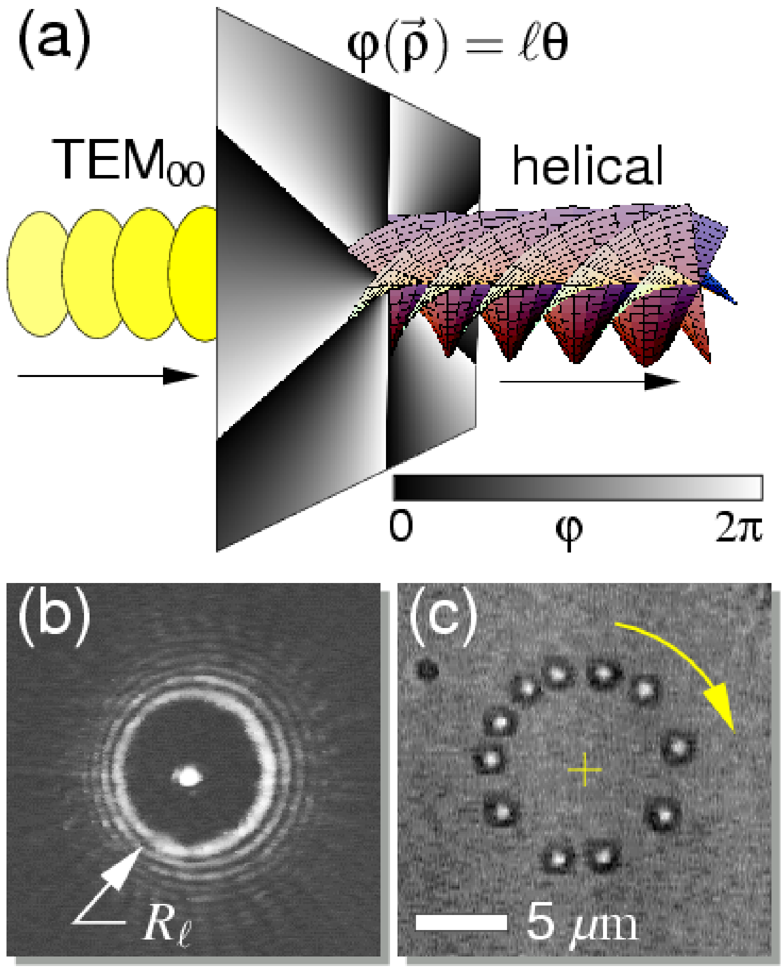

Fig. 3.1: (a)A TEM_{00} mode can be converted into a helical wavefront by adding a $\ell\theta$ azimuthal phase ramp around its axis of propagation. (b) A optical vortex can be generated by focusing a helical wavefront with specified topological charge ℓ. The radius of the optical vortex is directly related to the topological charge of the wavefront. (c) The orbital angular momentum carried by this mode of light can be transferred to illuminated particles either to make them rotate along the intensity maximum of the beam or to guide them along a designated trajectory as shown in [43]. Reprinted with permission from [44].

from redistributing the intensity distribution, helical modes' wavefront topology also redirects the light's momentum. The resulting spiral momentum converts into the beam with orbital angular momentum. A beam's orbital angular momentum depends only on its wavefront topology and is independent of its polarization. Linear polarized light that carries no spiral angular momentum still can carry orbital angular momentum. Apart from linear and spin angular momentum a helical wavefront carries rotational angular momentum. Such modes of light can be focused into optical traps to generate optical vortex. More sophisticated topological modes can even form knotted structures [47].

3.2 Applications of Topological Modes

Applications of topological modes of light was hindered by the difficulty of creating such modes using constrained optical elements such as mirrors and lenses. The introduction of diffractive optical elements effectively removed this barrieer and fostered a explosion of activity related to structured modes of light. The first widespread application of diffractive optics for beam shaping is the engraved into a plate of glass the Fresnel lens collects light from a large solid angle and collimates it into a beam without requiring a massive weight and size of a equivalent convex lens. The first such light shaping optics was installed in 1822. More recently, custom shaped laser beams have been used to address specific problems like in optical communication, photolithography, circuit component trimming, laser printing, optical data/image processing all of which requirement is that the light intensity is uniform over an area of cross-section [48]. A collimated beam of light which is equivalent to a truncated plane wave is ideal for all such applications.

One of the major challenges in the field of bio-medical optics is the limited range of imaging. Highly inhomogeneous distribution of refractive index inside a cell of most living organisms including human beings, reduces the spatial coherence of a light field. An added impurity to spatial coherence limits the ability to achieve diffraction limited focal spot size. Complex wavefront modulation to counteract such wavefront distortions due to propagation though turbid medium opens up new opportunities for optical micromanipulation in biological physics and also paves the way for super-resolution optical imaging. The idea of introducing adaptive optical elements to eliminate abberations is very well known in the field of astronomy [49, 50]. Wavefront shaping techniques used in adaptive optics system, adjust and sharpen any blurriness formed in the image of a star due to atmospheric perturbation of the light field. Similar technique is followed in biomedical optics where the phase of the wavefront is corrected using spatial light modulator.

Optical vortices are generated by focusing a mode of light with helical phase-ramp which is different than a regular point optical tweezers created from Gaussian beam. A uniform optical vortex can exert torque on a trapped particle through orbital angular momentum transfer. This property can be leveraged to utilize optical vortex as particle sorter between absorbing and non-absorbing particles [51–53]. Other desirable features of an optical vortex trap is its hollow structure and improved trapping efficiency in the axial direction [54]. Grier *et al.* [43] showed how multiple optical vortices can propel a polystyrene sphere along a specific trajectory in water. By changing the topological charge a dynamic optical vortex can be created with varying radius.

The orthogonality of optical modes with different topological charges makes modes of light with helical wavefront highly applicable for multiplexing to increase data capacity of both free-space and fiber-optic communications [55–58]. Strong variation in the electric field near the phase singularity "enables simultaneous single-spin imaging and magnetometry at the nanoscale with considerably less power than conventional techniques" [59].

3.3 Hermite-Gaussian and Laguerre-Gaussian Modes

The most common intended output of a laser cavity made by developers is a Gaussian beam. As its name implies Gaussian beam is an electromagnetic radiation whose transverse electric and magnetic amplitude profile is a Gaussian function. This Gaussian mode, which is also referred to as TEM_{00} mode, is one case of the generalized class of modes that are called "Hermite-Gaussian (HG) modes" which form a set of complete orthogonal basis functions that are also solutions of the paraxial Helmholtz equation in Cartesian coordinate system. The electric field of a HG mode, which is also denoted as $\mathrm{TEM}_{\ell m}$, can be written as:

$$\begin{aligned} E_{\ell,m}(x,y,z) = &E_0 \frac{w_0}{w(z)} H_\ell\left(\frac{\sqrt{2}x}{w(z)}\right) H_m\left(\frac{\sqrt{2}y}{w(z)}\right) \times \\ &\exp\left(-\frac{x^2+y^2}{w^2(z)}\right) \exp\left(-i\frac{k(x^2+y^2)}{2R(z)}\right) \exp(i\psi(z)) \quad , \end{aligned} \quad , \tag{3.1}$$

where E_0 is the normalization constant, w_0 is the diameter of the beam waist of the TEM_{00} mode, $w(z)$ and $R(z)$ are beam width and radius of curvature of

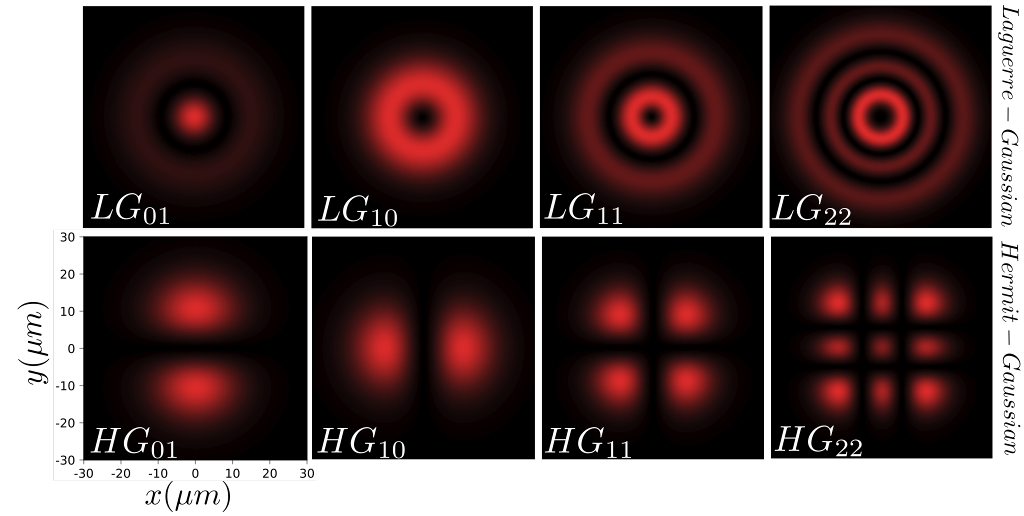

Fig. 3.2: Hermite-Gaussian (HG) and Laguerre-Gaussian (LG) beams are solutions of the paraxial Helmholtz equation for Cartesian and cylindrical coordinates, respectively. The top row shows a few example of LG beams which have rotational symmetry, while the HG beams have rectangular symmetry as shown in the bottom row.

the beam at an axial distance z away from the beam waist, $\psi(z)$ is the Gouy phase. $H_m(\cdot)$ is the Hermite polynomial [60] of order m. Because Hermite-Gaussian modes form the complete basis set of solutions to the paraxial Helmholtz equation, any arbitrary solution of the paraxial Helmholtz equation can be expressed as a superposition of multiple HG modes of light. A laser cavity with rectangular symmetry along the propagation axis can be adjusted to generate the family of HG beams. Many conventional strategies for generating topological modes of light, including helical modes atrt with Hermit-Gaussian modes and then impose special phase distributions with cyllindrical lenses or prisms.

In cylindrical coordinates the same electric field in Eq. (3.1) can be rewritten in terms of the generalized Laguerre polynomials. The associated basis functions are called Laguerre-Gaussian modes. Laser cavities with rotational symmetry produce such modes of light, where the electric field is written as:

$$\begin{aligned} E_{\ell p}(r,\phi,z) = & \frac{C^{LG}_{\ell p}}{w(z)}\left(\frac{r\sqrt{2}}{w(z)}\right)^{|\ell|}\exp\left(-\frac{r^2}{w^2(z)}\right)\times \\ & L_p^{|\ell|}\left(\frac{2r^2}{w^2(z)}\right)\exp\left(-ik\frac{r^2}{2R(z)}\right)\times \\ & \exp(-i\ell\phi)\exp(i\psi(z)) \quad , \end{aligned} \tag{3.2}$$

where $L_p^{\ell}(\cdot)$ are the generalized Laguerre polynomials and $C^{LG}_{\ell p}$ is a normalization constant. $w(z)$, $R(z)$ and $\psi(z)$ have the same interpretation as in Eq. (3.1). Like HG beams, LG beams form the complete set of orthogonal basis functions that are solutions to the paraxial Helmholtz equation in cylindrical coordinates. A circularly symmetric mode of light, which is a solution to Helmholtz equation, can be decomposed into the superposition of multiple LG beams. The family of Laguerre-Gaussian beams has a helical phase profile parametrized by the topologicql charge ℓ, and carries intrinsic orbital angular momentum of $\ell\hbar$ per photon [61] where ℓ is azimuthal mode index. In 1992 Allen *et al.* drew attention to the possibility that LG modes could transfer angular momentum to illuminated objects thereby exerting torques as well as force. This prediction and its subsequent experimental demonstration spread interest in singular optics and inspired experimental initiatives in atom guiding and optical trapping. Optical traps based on Laguerre-Gaussian modes are also known as "optical vortices"

Even though LG beams can be generated *in situ* with a laser cavity with rotational symmetry, small aberrations can lead to loss of mode purity. This is why HG modes have been the preferred basis for generating LG modes using conventional optical elements. In 1994 M.W.Beijersbergen *et al.* [46] showed experimentally how to convert a TEM_{00} mode into a helical wavefront using a spiral phase plate [62] which takes the form of a circular ramp of glass. These refraction mode convertors are difficult to fabricate and can be replaced by equivalent diffractive elements that are reminiscent of Fresnel lenses with a twist. Not only are helical diffractive optical elements comparatively easy to fabricate in glass, they lend themselves to implementation with liquid-crystal display technologies, opening up the possibility of dynamic topological modes.

3.4 Propagation Invariant Modes

One of the limitations of both HG and LG beams is their diverging property. Gaussian beams are not suitable for long-range optical micro-manipulation. Such long-range optical micro-manipulation requires the optical field to be propagation invariant [63]. A necessary condition of the wave field is the functional form of the transverse field distribution and the scale of intensity distribution remains unchanged in free-space propagation [64], although not necessarily with the same orientation [65]. By definition it is not a requirement for such modes of light to be continuously propagation invariant. A plane wave is the simplest example of a propagation invariant field which carries infinite amount of energy in the absence of a boundary. It is impossible to create such a field and added boundary condition becomes evident in the form of diffraction pattern as the plane wave propagated in free space. In 1987 Durnin [66] first presented a class of solution of paraxial Helmholtz equation, which are non-singular and the functional form of the transverse field in a plane is unaltered by propagating in free space. The simplest solution of this class of functions is:

$$\boldsymbol{E}(\boldsymbol{r}) = \exp(i\beta z)J_0(\alpha\boldsymbol{r}) \quad , \tag{3.3}$$

where J_0 is the zeroth order Bessel function of the first kind and α is a special parameter that determines the convergence angle of the plane waves that creates the Bessel field. One thing to notice in Eq. (3.3) is the functional form of the electric field does not have a boundary condition. The transverse intensity goes down as $O(1/r)$ as $r \to \infty$ which manifests as a infinite energy carrying wavefront similar to a unbounded planar wave. Therefore, even though it is a solution of the paraxial Helmholtz equation in free space, the field described in Eq. (3.3) is not realizable in real world. A finite version of Eq. (3.3) will be truncated at certain $r = R_0$ which limits the range of propagation invariance.

3.4.1 Bessel Beam

The time-dependent electric field of a generalized Bessel beam [64, 67] can be described as a complex field:

$$\boldsymbol{E}(\boldsymbol{r}, t) = J_m(k \sin\alpha\boldsymbol{r})e^{im\theta}e^{ik\cos\alpha z}e^{-i\omega t} \quad , \tag{3.4}$$

where J_m is the m$^{\text{th}}$ order Bessel function of the first kind, where m is an integer. $k = \sqrt{k_z^2 + k_r^2} = \frac{2\pi}{\lambda}$ is wavenumber, r, θ and z are the radial, azimuthal and longitudinal components respectively. α is a parameter that can take any value beteween 0 and π included. The amplitude of the Bessel beam has azimuthal symmetry and Eq. (3.4) satisfy the condition of propagation-invariant beam:

$$I(r, z \geqslant 0) = I(r) \quad , \tag{3.5}$$

where I is the transverse intensity of the beam.

Apart from $m = 0$ other Bessel beams carry orbital angular momentum which is unrelated to light's intrinsic linear and spin angular momentum. The amount of orbital angular momentum carried by individual photon is $m\hbar$, where m is an integer that can take negative values as well. The Bessel beams are all cylindrically symmetric and they form the complete basis set of orthogonal functions for an arbitrary cylindrically symmetric, propagation-invariant beam of light. The identity relation of Bessel function:

$$J_m(r) = \frac{i^{-m}}{2\pi} \int_0^{2\pi} e^{im\theta} e^{ir\cos\theta} d\theta \tag{3.6}$$

garners our attention to an alternative interpretation of the Bessel beam of light. It can be decomposed into plane waves propagating at an angle that forms a cone shape. The vertex angle of the cone:

$$\alpha = \tan^{-1} \frac{k_r}{k_z} \quad , \tag{3.7}$$

where k_r and k_z are radial and longitudinal wave-vectors respectively, determines the size of the center spot. The radius r_0 [67] of the center spot is related to α

through the relation:

$$r_0 = \frac{2.405}{k_z \tan \alpha}. \tag{3.8}$$

3.4.2 Other Propagation-Invariant Modes

There are two other classes of beams that fall into the same category of propagation-invariant modes of light. The first one was first proposed by Gutiérrez-Vega *et al.* [68] which is called "Mathieu beam". These modes of light are described by the radial and angular Mathieu functions. These are solution of the paraxial Helmholtz equation in the elliptical cylindrical coordinate system. The Mathieu beam of light propagates along elliptical trajectories. Another class of propagation-invariant mode is called "Weber beam" [69]. Unlike Mathieu beams, Weber waves propagate in parabolic trajectories. Airy beam is a special case of such modes of light.

These modes of light are also called accelerating modes of light due to their nonlinear path of propagation, which we talk in details in Ch. (5). While researchers have already experimentally created these mode of light, they are beyond the scope of this thesis because of their non-linear nature of propagation and difficult to create.

3.5 Optical Tweezers

Optical tweezers can impart customizable forces on the trapped colloidal particles. The ability to focus a laser beam tightly, to the diffraction limit, offers us the control to effectively trap a dielectric particle at length scales ranging from few

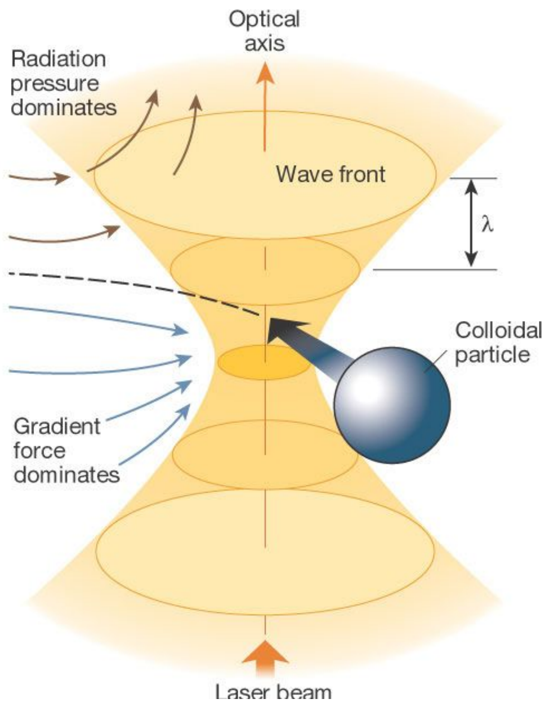

Fig. 3.3: A beam of light, tightly focused using a high numerical aperture creates a strong intensity gradient. It acts as an attractive force and drags small colloidal particles towards the focus spot. Whereas the radiation pressure repels the particle and push it away from the focal spot. When gradient force supersedes radiation pressure a stable optical trap is created and a particle can be trapped in three dimension near the focal spot. Picture taken with permission from David G. Grier [44]

nanometers to millimeters. In 1986 Arthur Ashkin and his co-workers [30] from Bell laboratories for the first time reported how a single beam can be tightly focused to create a strong gradient force to trap particles. Due to this pioneering experiment and his contribution in the field of optical tweezers Arthur Ashkin won the 2018 Nobel Prize in Physics[70]. Since the inception, many physicist and biologist have shown the versatility of this technique[44]. The optical force on a trapped object can be controlled at an $\sim$ 100aN precision between $\sim$ 1pN to a few $\sim$ 100pN [71]. Such range of force is optimal for probing biological systems, ranging from single molecule biophysics to measuring responses in macromolecular systems[72–74]. Svoboda *et al.* [75] has studied single molecules of the motor protein kinesin, moving under low mechanical loads at saturating ATP concentrations. Mondal *et al.* [76] has discovered how weakly focused beam can be used for highly efficient axonal guidance in a non-invasive manner. Outside of biological applications, optical tweezers have been used in myriad of studies for example, to measure pair interaction potential of charge-stabilized colloid [77], for characterizing and tracking single colloidal particles [78–82].

3.6 Holographic Optical Trapping

In Holographic Optical tweezers the wavefront of a single light beam is modified using a computer generated hologram to create different mode structures. If you look back at Eq. (2.8) the optical field can be controlled either by changing the amplitude $u(\boldsymbol{r})$ or by modifying the phase $\phi(\boldsymbol{r})$. In our present setup we utilize a phase-only Spatial Light Modulator (SLM) [83] to adjust the phase of the field in a plane as it is described in [84–88]. A schematic of our experimental setup is shown in Fig. 3.4

We use a linearly polarized laser at a wavelength of 532nm from Coherent Verdi 5W as our trapping laser. The initial diameter of the laser beam is less than 2mm. It passes through a 5X beam expander before it incidents on the phase-only SLM (Hamamatsu $X10468-16$). The 5X beam expander makes the beam

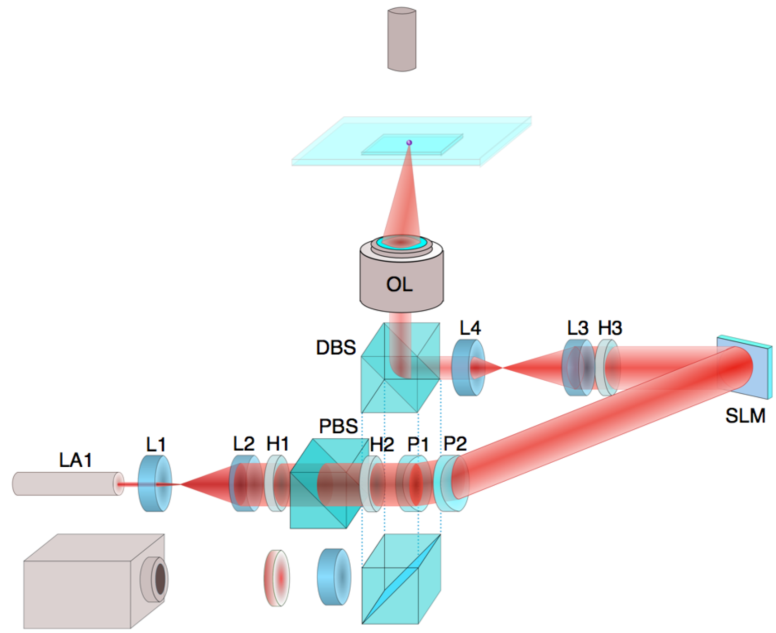

Fig. 3.4: Schematic of HOT setup. Permission: copied from Bhaskar's thesis, will make my own

uniform and overfills the aperture (15.8mm $\times$ 12mm) of the SLM. The incident angle is maintained at less than 5° in order to retain the maximum light utilization efficiency (96%) of the reflective SLM. The SLM has a 1920 $\times$ 1080 pixels liquid crystal screen which limits the resolution of the computer generated holograms that can be imprinted on the light field. The resultant light from the SLM then goes through a telescopic $(4 - f)$ system before going through the objective lens. Depending on trapping requirements, we use a high numerical aperture (NA) oil immersion objective (Nikon Plan-Apo 100X; NA 1.4). Finally the light is focused inside the sample chamber, which for our purpose consist of water solution of colloidal particle of $\sim 2\mu$m in diameter.

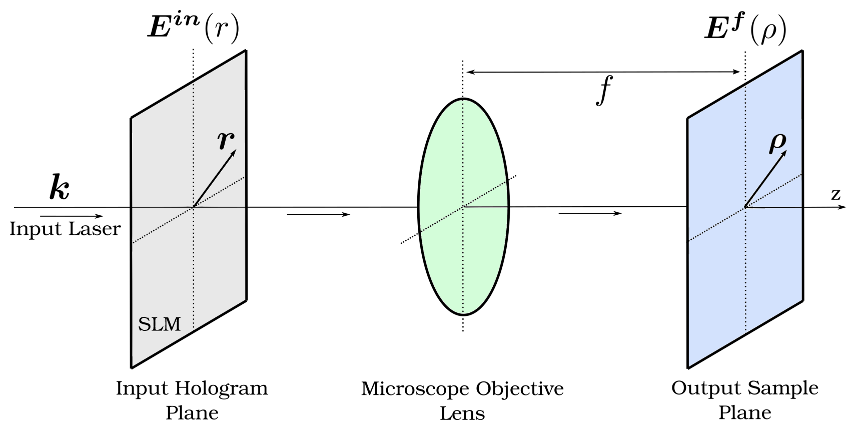

Fig. 3.5: In order to create a specific mode of light with electric field $\boldsymbol{E}^f(\boldsymbol{\rho})$ on the sample plane using digital holography, we need to project a phase in the input hologram plane that will transform the Laser field into $\boldsymbol{E}^{in}(\boldsymbol{r})$. Due to the specific configuration of the setup shown in this schematic $\boldsymbol{E}^f(\boldsymbol{\rho}) = \mathcal{F}\{E^{\text{in}}(\boldsymbol{r})\}$.

3.7 Phase-Only Holograms

The experimental setup shown in Fig. 3.4 can be simplifed into Fig. 3.5 in order to understand the relation between the optical field in the SLM plane and the field in the sample plane. In the paraxial limit the lens acts as a Fourier transform operator [16]. The electric field in the focal plane ($E^f(\boldsymbol{\rho})$) of the objective lens is related to the field in the hologram plane ($E^{\text{in}}(\boldsymbol{r})$) by:

$$E^f(\boldsymbol{\rho}) = -\frac{i}{\lambda f}\int dr^2 E^{\text{in}}(\boldsymbol{r}) \exp\left(-i\frac{k}{f}\boldsymbol{r}\cdot\boldsymbol{\rho}\right) \quad , \tag{3.9a}$$

$$\equiv \mathcal{F}\{E^{\text{in}}(\boldsymbol{r})\} \quad \text{and} \tag{3.9b}$$

$$E^{\mathrm{in}}(\boldsymbol{r}) = \mathcal{F}^{-1}\{E^{f}(\boldsymbol{\rho})\} \tag{3.10}$$

where f is the focal length of the objective lens and $\boldsymbol{r}$ and $\boldsymbol{\rho}$ are the position vectors on the hologram plane and on the focal plane respectively. Therefore, in order to obtain a desired electric field in the focal plane we need the inverse Fourier transformed electric field in the hologram plane. Now to get $E^{\mathrm{in}}(\boldsymbol{r})$ from the incident laser field $E_0(\boldsymbol{r}) \equiv u_0(\boldsymbol{r})e^{i\phi_0(\boldsymbol{r})}$ we need to modify both amplitude and the phase of the input field in the hologram plane. While several research groups have devised ways to modify the amplitude [89–94] using phase-only SLM, for our purpose such techniques do not improve the mode quality by reasonable amount. Let us assume, in order to obtain the desired electric field $F^{r}(\boldsymbol{\rho})$ we need to transform incident laser field $E_0(\boldsymbol{r})$ into $E^{\mathrm{in}}(\boldsymbol{r}) = u^{\mathrm{in}}(\boldsymbol{r})\exp(ik\phi^{\mathrm{in}}(\boldsymbol{r}))$ in the hologram plane. We overfill the SLM aperture in order to make the assumption $u_0(\boldsymbol{r}) = 1$. Using our phase-only SLM we can transform the phase of the incident field $\phi_0(\boldsymbol{r})$ into $\phi_{\mathrm{in}}(\boldsymbol{r})$. Therefore we end up with a residual electric field equal to the second term of Eq.(3.11)

$$\begin{aligned} e^{\phi_{\mathrm{in}}(\boldsymbol{r})} \quad &= \quad u^{\mathrm{in}}(\boldsymbol{r})e^{ik\phi^{\mathrm{in}}(\boldsymbol{r})} && (3.11a) \\ &\quad + \left(1 - u^{\mathrm{in}}(\boldsymbol{r})\right) e^{ik\phi^{\mathrm{in}}(\boldsymbol{r})} && (3.11b) \end{aligned}$$

In order to prevent any interference between these two terms in Eq. (3.11) we deflect the desired light field by adding an additional phase ramp [86] equal to

:

$$\phi_{\mathrm{disp}}(\boldsymbol{r}) = \frac{k}{f}\boldsymbol{\rho_0} \cdot \boldsymbol{r} \tag{3.12}$$

to certain location.

Chapter 4

Projecting Long Range Non-Diffracting Waves

4.1 Tractor Beam: A Special Case of Non-Diffracting Waves

The term “Tractor beam” was coined by Steven Block in 1992 [95] and was originally attributed to optical tweezers for their ability to trap microscopic particles and transport then in controlled fashion. However further investigation revealed an optical tweezers or a point trap does not qualify as a beam of light that can transport an object long distance because of its limited range of applicability. Therefore the definition has since been updated; tractor beams are a class of optical modes which are traveling waves that transports objects back to its source, opposite to the direction of propagation. Following Eq. (2.24) the force field of a mode of light needs to satisfy the condition:

$$\boldsymbol{F}_z \cdot \boldsymbol{z} < 0 \tag{4.1}$$

to become a tractor beam. It can impart a conservative force on the object towards the direction of the source. In this sense an optical tweezers is not a tractor beam. In 2005 **Ciz**már *et al.* [96] presented optical conveyor belt which can transport submicron objects over a distance of 250 µm. Even though it has a long range of transportability, this mode of light "is based on a standing wave (SW) created from two counter-propagating nondiffracting beams where the phase of one of the beams can be changed. [96]" and therefore it is not a tractor beam by our definition. One sided tractor beam was experimentally demonstrated by Ruffner *et al.* [97] which was created by coherently superposing coaxial Bessel beams.

Because Bessel functions form a complete set of orthogonal basis functions which are solutions to the paraxial Helmholtz equation, any propagation invariant or linear non-diffracting mode of light can be expressed as a linear superposition [97–99] of Bessel beams. In the force calculation for a single Bessel beam using Eq. (2.24) it is evident that the z-component of $\boldsymbol{F_e}(\boldsymbol{r})$:

$$\partial_z \sum_{j=0}^{j=2} u_j^2(\boldsymbol{r}) = 0 \tag{4.2}$$

as the transverse intensity distribution remains unchanged for a Bessel beam. For a pure dielectric particle, which does not absorb light the second term in Eq. (2.24) is also 0 because $\alpha_e'' = 0$. Even for absorbing particles with $\alpha_e'' > 0$ the second term

$$\alpha_e'' \sum_{j=0}^{2} u_j^2(\boldsymbol{r}) \partial_z \phi_j(\boldsymbol{r}) > 0 \tag{4.3}$$

is non-negative. Therefore a single Bessel beam cannot act as a tractor beam as it is evident from the force calculation using Eq. (2.24). However, it is possible to construct a mode of light by superposing different Bessel beams which can act as a long range propagation-invariant tractor beam that will pull objects upstream towards the source of light. The simplest superposition will be two Bessel beams with the similar axis of symmetry and are mutually coherent. The electric field of such a superposed mode of light:

$$E(\boldsymbol{r}, \theta) = a_1 E_{\alpha,m}(\boldsymbol{r}, \theta) + a_2 E_{\alpha',m'}(\boldsymbol{r}, \theta) \quad , \tag{4.4}$$

where a_1, a_2 are arbitrary scalar amplitudes, α,α' are two different convergence angles, and m,m' characterizes orbital angular momentum of different order Bessel beams.

4.1.1 Conveyor Beam

Following Eq. (4.4), an optical Conveyor beam is a superposition of two 0th order Bessel beams i.e. $m = m' = 0$. While the superposing Bessel beams do not carry any orbital angular momentum, due to different convergence angles, α, α' they interfere and create a periodic amplitude maximum and minimum along the axis of symmetry. If $a_1 = a_2 = 1$ the electric field along the axis ($\boldsymbol{r} = 0$) becomes a periodic function:

$$E(z) = 2\cos\left(kz\frac{\cos\alpha - \cos\alpha'}{2}\right)\exp\left(ikz\frac{\cos\alpha + \cos\alpha'}{2}\right) \quad , \tag{4.5}$$

where the alternative bright and dark spots occur at a period of:

$$\triangle\ z = \frac{2\pi}{k\left(\cos\alpha - \cos\alpha'\right)} \quad . \tag{4.6}$$

Particles can be trapped in each on the array of intensity maximums and and transported upstream or downstream along the axis of the conveyor beam by selectively altering the relating phase of the interfering Bessel beams. The axial transport velocity of the trapped particle depends on the rate of change in the relative phase of the two Bessel beams, which can be written as:

$$v(t) = \frac{\triangle\ z}{2\pi}\frac{\partial\phi(t)}{\partial t} \quad , \tag{4.7}$$

where $\phi(t)$ is the time dependent change in phase difference between the two interfering Bessel beams. A detailed force calculation was reported in [97] and it suggests conveyor beam can act as a tractor beam irrespective of a particle's characteristics. While particles with refractive index relative to the medium greater than one will be trapped in the intensity maximum, dark-seeking i.e. particles whose relative refractive index is less than one, will find the local intensity minimum as the stable point.

4.1.2 Solenoidal Beam

A solenoid beam is where the intensity maximum spirals around the axis of propagation. Similar to a conveyor beam it is a solution of the Helmholtz equation in the paraxial limit and it is a superposition of multiple Bessel beams. The spiraling intensity profile of a solenoid beam is discreetly propagation invariant mode of light along its axis of propagation, which can be written as:

$$I\left(\boldsymbol{r},\theta,z\right)=I\left(\boldsymbol{r},\theta,z+\triangle\, z\right)\quad , \tag{4.8}$$

but the radial intensity profile remains unchanged in the spiraling frame of reference [100]. First experimental realization of a solenoid beam presented in [99] describes it as a superposition of a finite series of Bessel beams given by:

$$\boldsymbol{E}_{\gamma,l}(\boldsymbol{r},z)=\sum_{m=[l-\gamma k]}^{[l]}\frac{l-m}{\gamma^2}J_m(q_mR)e^{i\frac{l-m}{\gamma}z}e^{im\theta}J_m(q_mr)\quad , \tag{4.9}$$

where γ is the pitch of the spiral intensity profile and R is the radius. Figure. 4.1 shows how the wavefronts update with changing helical pitch l from Eq. (4.9). For $l<0$ (e.g. Fig. 4.1(c) where $l=-40$) the phase gradient force acts as a pulling force which moves trapped objects upstream. However, the simplest superposition of two coherent Bessel beams like in Eq. (4.4) can also generate a solenoidal beam. These two Bessel beams interfere coherently and produce intensity maximum wherever the following condition is satisfied:

$$(m\theta+k\cos\alpha z)-(m'\theta+k\cos\alpha' z)=2n\pi\quad , \tag{4.10}$$

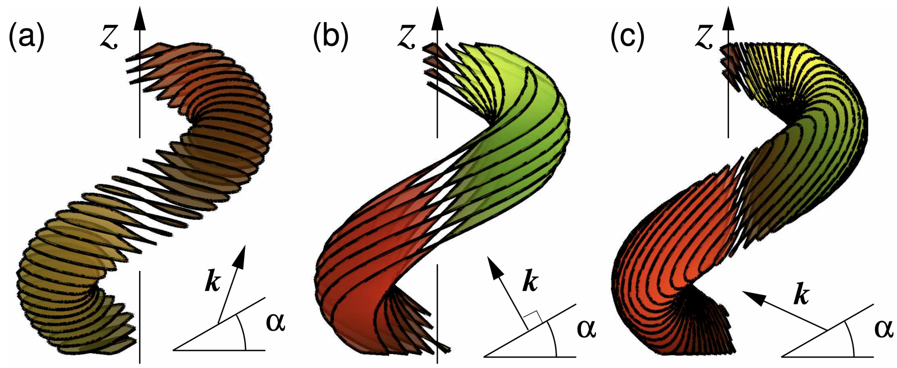

Fig. 4.1: Retrograde forces in a helical solenoid beam. The local wave vector k is normal to the light's wavefronts, with a component in the $\hat{z}$ direction. (a) $l = +40$: $\boldsymbol{k}$ is directed along the solenoid, resulting in a downstream phase-gradient force. (b) $l = 0$: Wavefronts are parallel to the solenoid so that k is everywhere normal to the spiral. Particles trapped by intensity-gradient forces experience no net force. (c) $l = -40$: A component of $\boldsymbol{k}$ is directed back down the spiral. A particle confined to the spiral therefore moves upstream. Source: Reprinted with permission from [99].

where n is a non-negative integer. The intensity maximum traces a helical path which can be presented in the azimuthal axis as a function of axis of propagation z as:

$$\theta_0(z) = \frac{kz\,(\cos\alpha - \cos\alpha')}{m - m'}. \tag{4.11}$$

By changing the orbital angular momentum (m,m') or the angle of convergence (α,α') of individual Bessel beams we can control pitch (γ) and radial distance of the intensity maximum of a solenoid beam. For an example, if we wish to create a solenoid beam with intensity maximum at $r = R$ which is formed due to superposition of ν-th maximum of J_m and ν'-th maximum of $J_{m'}$ we need to ensure

$$\frac{\sin\alpha}{j'_{m,\nu}} = \frac{\sin\alpha'}{j'_{m',\nu'}} = \frac{1}{kR} \quad , \tag{4.12}$$

where $x = j'_{m,\nu}$ is the ν-th root of $J'_m(x) = 0$. In this simplistic model, the value of γ(introduced in Eq. (4.9)) is:

$$\gamma = \frac{2\pi}{k}\frac{m - m'}{\cos\alpha - \cos\alpha'} \tag{4.13}$$

and there are $|m - m'|$ maxima in the transverse intensity profile. In Eq. (4.13) modifying either numerator or denominator in a way to change the overall sign of γ will change the circular handedness of the helical solenoid beam. The intensity maximum at $r = R$ generates a intensity gradient force which pulls objects towards the spiral potential minimum and creates a effective optical trapping in the radial direction. Phase gradient propels the particle in the axial direction. Under this

$$m'\cos\alpha > m\cos\alpha' \tag{4.14}$$

constraint, the solenoid beam acts as a tractor beam which also makes $\nu' > \nu$ a necessary condition for retrograde force. Conditions from Eq. (4.12) and Eq. (4.14) can be used to find out

$$\sin^2\alpha < \frac{\left(\frac{m^2}{m'^2} - 1\right)}{\left(\frac{m^2}{m'^2} - \frac{j'^2_{m,\nu}}{j'^2_{m',\nu'}}\right)} \tag{4.15}$$

in order for the beam of light to act as a tractor beam.

4.2 Projecting Bessel Beam with Digital Hologram

Holograms intended for optical micromanipulation typically are designed to modify the phase profile of an incident laser beam, but not the amplitude. The phase-only hologram then propagates to a converging lens that transforms it into the intended mode. Scalar diffraction theory approximates this transformation as a Fourier transform [101] as described in described in Sec. 3.6 and Sec. 3.7. Difficulties are encountered when the Fourier transform of the desired mode features amplitude variations that can not be encoded naturally in a phase-only diffractive optical element.

For example, the ideal complex-valued hologram encoding an m-th order Bessel beam as mentioned in Eq. (3.4), the input electric field on the hologram plane has to be same as Eq. (3.10) which takes the form of an infinitesimally fine ring,

$$E_{\alpha,m}(\boldsymbol{r},0) = \delta(r - R_\alpha)\, e^{im\theta}, \tag{4.16}$$

whose radius,

$$R_\alpha = f\ \tan\alpha \quad , \tag{4.17}$$

depends on the focal length of the projecting lens, f as shown in the schematic Fig. 3.5, and the desired convergence angle of the Bessel beam, α. α is correlated with the center spot size and propagation invariant range of the Bessel beam as discussed in Sec. 3.4.1. Equation (4.16) expresses the scalar field in terms of the two-dimensional polar coordinates, $\boldsymbol{r} = (r,\theta)$, in the plane $z = 0$. More generally,

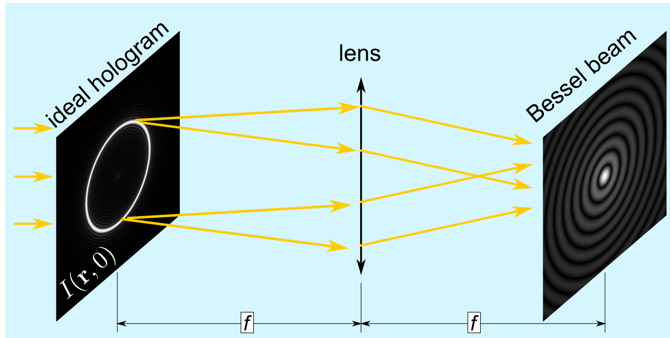

Fig. 4.2: Conventional holographic projection of a Bessel beam. The field diffracted by a ring hologram propagates to a converging lens of focal length f that projects it into the non-diffracting mode.

$E_{\alpha,m}(\boldsymbol{r}, z)$ describes the transverse profile of the same field at axial position z.

The ideal ring hologram consists of an amplitude mask, shown schematically in Fig. 4.2, that only allows light to pass through the thin annulus at radius R_α, and a phase mask that imposes a helical pitch on the transmitted wavefronts. The same effect can be achieved with a phase-only hologram,

$$\varphi_{\alpha,m}(\boldsymbol{r}) = \begin{cases} m\theta \bmod 2\pi, & r = R_\alpha \\ \varphi_0(\boldsymbol{r}), & \text{otherwise} \end{cases} \tag{4.18}$$

where $\varphi_0(\boldsymbol{r})$ is an unspecified phase function that diverts light away from the axis [102].

Equation (4.18) poses two substantial problems for standard holographic trapping implementations of the kind represented in Fig. 4.2. In the first place, the delta-function amplitude profile in the hologram plane cannot be encoded faithfully on a pixelated diffractive optical element. The bright ring in Fig. 4.2 represents the intensity, $I(\boldsymbol{r}, 0) = |E_{\alpha,0}(\boldsymbol{r}, 0)|^2$, projected by an $m = 0$ ring holo-

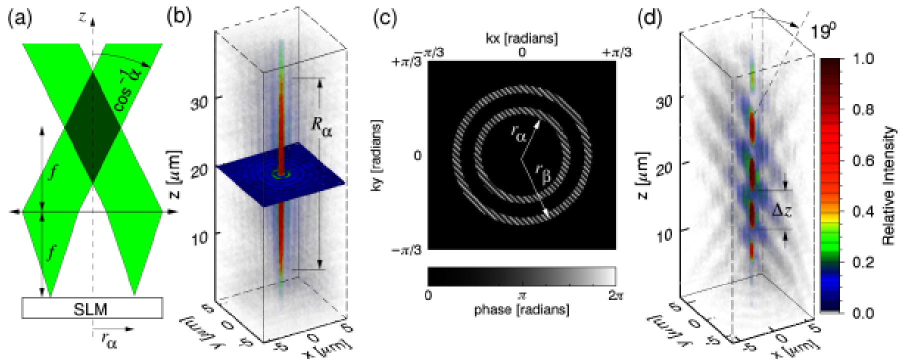

Fig. 4.3: (a) Schematic representation of holographic projection of a Bessel beam with axial wavenumber αk by a lens of focal length f. Shaded region indicates volume of invariant propagation. (b) Volumetric reconstruction of a holographically projected Bessel beam. (c) Phase hologram encoding an optical conveyor. Diagonal blazing tilts the projected conveyor away from the optical axis. (d) Volumetric reconstruction of the beam projected by the hologram in (c). The color bar indicates relative intensities in (b) and (d). Source: Reprinted with permission from [103].

gram, treated as an ideal amplitude mask. The ring's finite thickness arises from the mask's finite pixel size. Rather than projecting a wave with a single value of α, this finite-thickness ring constitutes a superposition of ring holograms that corresponds to a superposition of Bessel beams with a range of convergence angles. Interference among these superposed modes causes periodic axial intensity variations, and so limits the propagation-invariant range of the superposition [103] as shown in Fig. 4.3(b). Figure. 4.3(d) shows a conveyor beam created by using a digital hologram that encodes two Bessel beam as a ring with certain thickness. Using this method constraints the propagation invariant range to the order of 100 μm

In the second place, only a few pixels in the hologram plane contribute to the intended Bessel beam. The rest of the hologram's area is dedicated to the phase function $\varphi_0(\boldsymbol{r})$ that diverts extraneous light away from the desired mode. Pixelated ring holograms thus suffer from a combination of poor mode fidelity and extremely poor diffraction efficiency.

4.3 Intermediate Plane Holography

Structuring laser beams with computer-generated holograms has created revolutionary opportunities for optical micromanipulation [104] and optical communication [105–107]. Using holograms to project propagation-invariant modes of light, for example, has led to the remarkable discovery that some non-diffracting modes can act as tractor beams, pulling illuminated objects upstream rather than trapping them or pushing them downstream [108, 109]. Applications of tractor beams and other exotic light modes have been hampered by the poor diffraction efficiency of the holograms used to project them, which can be less than 10^{-3} [103, 110]. To address this problem, we introduce intermediate-plane holography, which can dramatically improve both diffraction efficiency and mode purity. We illustrate these capabilities by projecting Bessel beams, which constitute the natural basis for propagation-invariant modes [5, 6]. We then use these techniques to project meter-long optical conveyors [103, 110, 111] and solenoid beams [109, 112], which are tractor-beam modes composed of superpositions of Bessel beams. These experiments demonstrate a 400-fold improvement in diffraction efficiency relative to the standard holographic optical trapping technique, and a 100-fold increase in non-diffracting range.

Both deficiencies mentioned in Sec. 4.2 can be mitigated by considering light's propagation from the hologram plane to the converging lens. The field at distance z along the optical axis may be estimated with the Rayleigh-Sommerfeld diffraction integral [113],

$$E(\boldsymbol{r}, z) = \int \tilde{E}(\boldsymbol{q}, 0)\tilde{H}_z(\boldsymbol{q})e^{-i\boldsymbol{q}\cdot\boldsymbol{r}}\, d^2q, \tag{4.19a}$$

where $\tilde{E}(\boldsymbol{q}, 0)$ is the Fourier transform of the field $E(\boldsymbol{r}, 0)$ in the plane $z = 0$ and

$$\tilde{H}_z(\boldsymbol{q}) = e^{iz\sqrt{k^2-q^2}} \tag{4.19b}$$

is the Fourier transform of the Rayleigh-Sommerfeld propagator for light of wave number k [101]. Because the light diffracts as it propagates, challenging amplitude variations in $E(\boldsymbol{r}, 0)$ can be substantially less pronounced in the intermediate plane at axial position z. This can be seen in the intermediate-plane intensity, $I(\boldsymbol{r}, z) = |E_{\alpha,0}(\boldsymbol{r}, z)|^2$, for the $m = 0$ mode in Fig. 4.4. A phase-only hologram designed for this plane therefore will have much better diffraction efficiency than the ideal hologram designed for $z = 0$. Indeed, the location, z, of the intermediate plane can be selected to maximize this benefit. Improving diffraction efficiency naturally improves mode fidelity by reducing the amount of light in unwanted modes. Performance may be even better than this observation suggests because $E(\boldsymbol{r}, z)$ is computed from the ideal field, without compromise for pixelation.

The phase-only intermediate-plane hologram associated with $E(\boldsymbol{r}, 0)$ may be approximated by the phase, $\varphi(\boldsymbol{r}, z)$, of $E(\boldsymbol{r}, z)$, ignoring amplitude variations. The intermediate-plane phase for the $m = 0$ Bessel beam is presented in Fig. 4.5(b). If necessary, some accommodation may be made for remaining amplitude variations

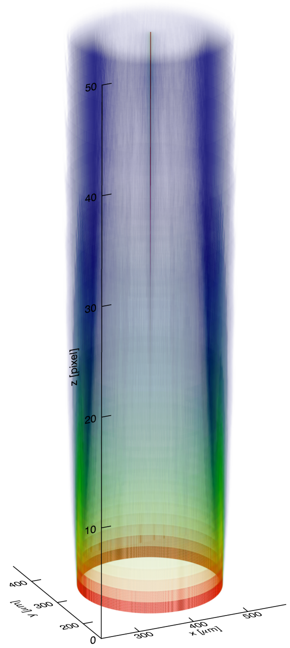

Fig. 4.4: The electric field intensity distribution becomes smoother as we move from $z = 0$ to an intermediate plane. This figure shows a volumetric reconstruction of the electric field intensity computed using Rayleigh-Sommerfeld propagator.

through any of the techniques that have been developed for encoding complex-valued fields on phase-only diffractive optical elements [102]. In practice, this often is unnecessary, and the phase of the computed intermediate-plane field serves as a mode-forming hologram with high diffraction efficiency.

The benefits of intermediate-plane holography come at a cost. Specifically, the diffractive optical element no longer is located in the focal plane of the projecting lens. This requires modifying the optical layout of a typical holographic trapping system. For the particular case of reflective holograms, space constraints

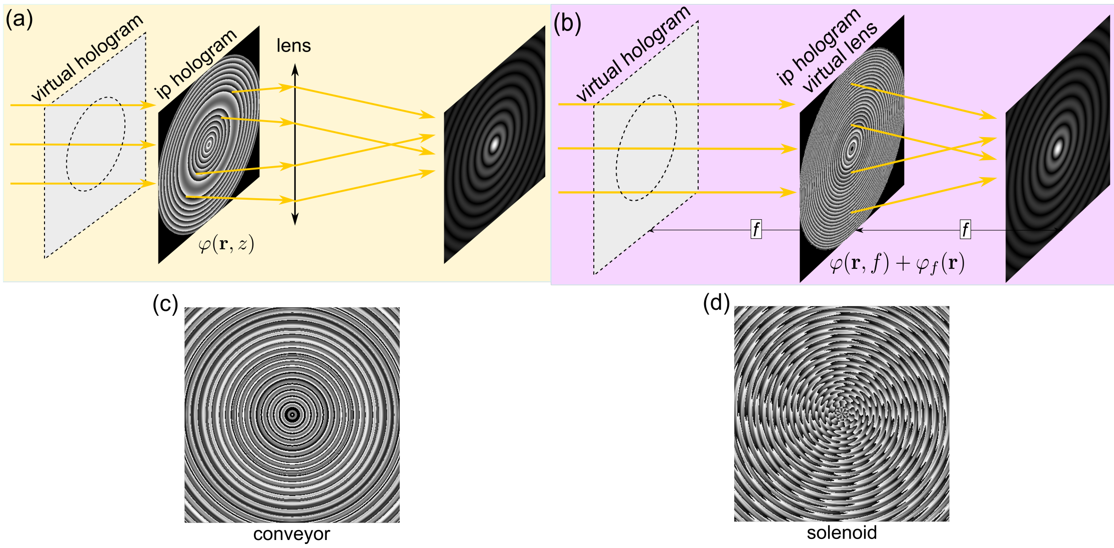

Fig. 4.5: Intermediate-plane holography. (a) A phase-only hologram in an intermediate plane recreates the ring-hologram's wavefront structure at substantially higher diffraction efficiency. (b) Moving the intermediate plane to $z = f$ and incorporating the phase function for the converging lens creates a mode converter that projects the Bessel beam directly. Intermediate-plane phase holograms for (c) an optical conveyor and (d) a solenoid beam. The beams projected by these holograms are shown in Fig. 4.9.

may limit the range of z, and thus the benefit of the technique. In cases where large positive values of z are physically inaccessible, negative values may offer the same benefits while affording sufficient space for practical implementation.

Setting $z = f$ addresses these geometric considerations by placing the intermediate-plane hologram in the same plane as the converging lens. The associated parabolic phase profile,

$$\varphi_f(\boldsymbol{r}) = \frac{\pi r^2}{\lambda f} \bmod 2\pi, \tag{4.20}$$

can be integrated into the phase function for the intermediate-plane hologram,

$$\varphi(\boldsymbol{r}) = [\varphi(\boldsymbol{r}, f) + \varphi_f(\boldsymbol{r})] \bmod 2\pi, \tag{4.21}$$

thereby eliminating the need for the physical lens altogether. This mode of operation is presented in Fig. 4.5(b) and is the approach we will adopt for experimental demonstrations.

For the particular case of a Bessel beam, the Fourier transform of the ideal ring hologram is

$$\tilde{E}_{\alpha,m}(\boldsymbol{q}, 0) = J_m(qR_\alpha)\, e^{im\theta}. \tag{4.22}$$

Applying Eq. (4.19) then yields an expression for the field in the intermediate plane,

$$E_{\alpha,m}(\boldsymbol{r}, z) = e^{im\theta} \int_0^k qJ_m(qr)J_m(qR_\alpha)\, e^{iz\sqrt{k^2-q^2}} dq, \tag{4.23}$$

whose phase is the first-order approximation to the intermediate-plane phase hologram encoding the Bessel beam. The upper limit of integration in Eq. (4.23) ignores exponentially small contributions from terms with $q > k$ because $kz \gg 1$ in practice. Due to unknown solution of the integral form in Eq. (4.23) we switch to the inverse Fourier Cartesian coordinate space as used in the Fresnel approximation of Rayleigh-Sommerfeld equation in Eq. (2.18). Unlike far field approximation pointed out in Eq. (2.19) this approximation is not valid in intermediate-plane holography. The idea is to retain as much information as possible while reducing the rate of amplitude modulation so that the second term in Eq. (3.11) is small or negligible.

Following the schematic in Fig. 4.6, the electric field on plane $z = z$ will

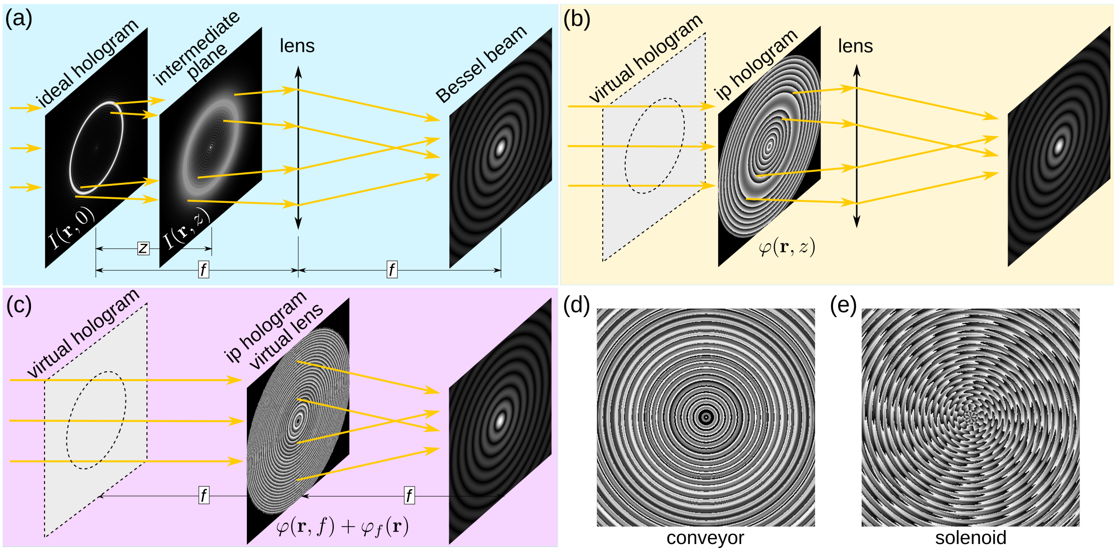

Fig. 4.6: [MAKE THE RIGHT IMAGE XXXXXXX] Schematic Intermediate-plane field calculation.

be,

$$U(x,y,z) = \frac{i}{\lambda}\int_{x',y'} U(x',y',0)\cos\phi' \frac{\exp{(ik\ell)}}{\ell} dx'dy' \quad . \tag{4.24}$$

$\cos\theta'$ can be written in terms of z and ℓ as

$$\cos\phi' = \frac{z}{\ell} \tag{4.25}$$

which yields,

$$U(x,y,z) = \frac{i}{\lambda}\int_{x',y'} U(x',y',0)\frac{z}{\ell^2}\exp{(ik\ell)}\,dx'dy' \quad . \tag{4.26}$$

In Cartesian coordinate ℓ can be written as:

$$\ell^2 = (x-x')^2 + (y-y')^2 + z^2 \quad , \tag{4.27}$$

and $\rho = x^2 + y^2 + z^2$. We can rewrite ℓ from Eq. (4.27) in terms of ρ as

$$l = \rho - \frac{xx' + yy'}{\rho} + \frac{x'^2 + y'^2}{2\rho} + \mathcal{O}\{\frac{x^2 x'^2}{\rho^3}, \frac{y^2 y'^2}{\rho^3}\} \tag{4.28}$$

Moving to polar coordinate from Cartesian coordinate such that

$$(x', y') \equiv (\eta, \phi) \quad , \tag{4.29a}$$

$$(x, y) \equiv (r, \theta) \quad , \tag{4.29b}$$

we can rewrite Eq. (4.26) as

$$U(r, \theta) = \frac{i}{\lambda} \frac{z}{\rho^2} \int U(\eta, \phi) \exp\left[-\frac{ik}{\rho}\left(r\eta\cos(\theta - \phi) - \eta^2\right)\right] d^2\eta \tag{4.30}$$

In order to produce a Bessel beam in (r, θ) plane we need

$$U(\eta, \phi) = \delta(\eta - R_\alpha) \quad , \tag{4.31}$$

where R_α is the radius of the delta ring similar to what is mentioned in Eq. (4.16). Replacing $U(\eta, \phi)$ with Eq. (4.31) in Eq. (4.30) yields:

$$U(r, \theta) = \frac{i}{\lambda} \frac{R_\alpha z}{\rho^2} \exp\left[i\left(k\rho + \frac{k}{\rho} R_\alpha^2\right)\right] \int_0^{2\pi} e^{-i\frac{k}{\rho} R_\alpha r \cos(\theta - \phi)} d\theta \tag{4.32}$$

Equation (4.32) can be computed analytically for arbitrary α and m. In the limit $z > R_\alpha$, it reduces to

$$E_{\alpha,m}(\boldsymbol{r}, z) \approx \beta^2 \, e^{-i\frac{kr^2}{2z}} \, e^{ikR_\alpha\left(\beta + \frac{1}{\beta}\right)} \, J_m\left(\beta \, kr\right) \, e^{im\theta}, \tag{4.33a}$$

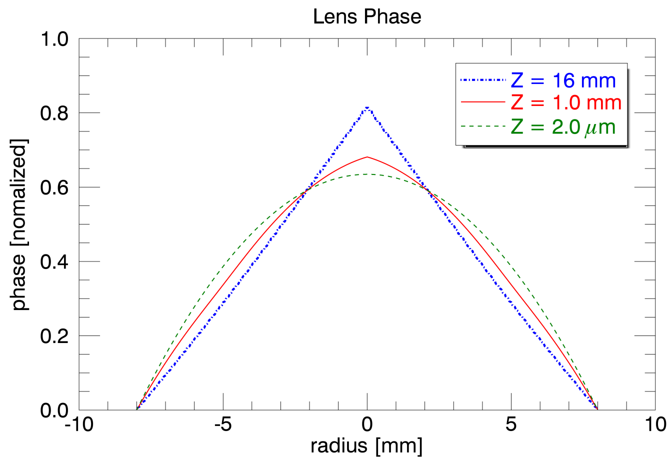

Fig. 4.7: The figure shows how the phase changes as we change the depth of the intermediate plane for projecting the hologram. At $z \gg R_\alpha$ the phase reduces to the phase profile of an axicon, which is the physical way to create a Bessel beam from a collimated beam of coherent light.

where

$$\beta = \frac{R_\alpha}{\sqrt{r^2 + z^2}}. \tag{4.33b}$$

The single-element mode converter,

$$E_{\alpha,m}(\boldsymbol{r}) = E_{\alpha,m}(\boldsymbol{r}, f)\, e^{i\varphi_f(\boldsymbol{r})}, \tag{4.34}$$

has a phase profile that, in turn, reduces to the conical profile of an axicon as shown in Fig. 4.7 in the long-range limit, $z \gg R_\alpha$.

An axicon's departure from the profile in Eq. (4.33) can reduce the mode

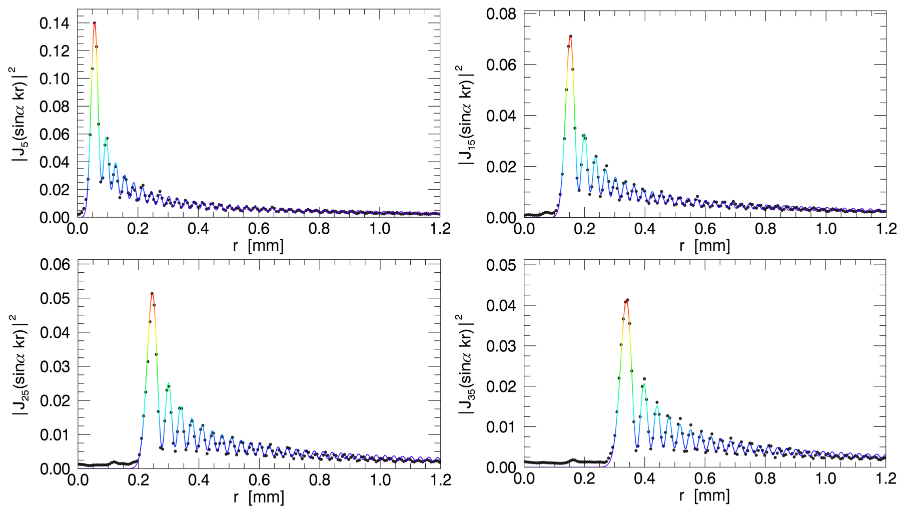

Fig. 4.8: Higher order Bessel beams J_5, J_{15},J_{25}, and J_{35} are created using intermediate plane holography for $z = 54\,\mu\mathrm{m}$. The black solid line is the best non-linear fit of the intensity distribution of the Bessel beams. Perfect overlap of experimental and analytical solution suggests high mode purity of the generated modes of light.

purity and non-diffracting range of the beams it projects. Physical axicons have the further problem that their tips cannot be infinitely sharp. Rounding introduces mode artifacts that also reduce the propagation-invariant range [114].

Another point to consider while choosing the optimum z is the rate of change of phase in plane (r, θ). For a constant $r = R_0$ the maximum phase $\varphi_{\max} \propto \frac{1}{z^2}$, which limits the ability to encode a phase in a phase only SLM with finite sized pixels.

Figure. 4.8 shows higher order Bessel beams created with a phase hologram computed from the intermediate plane electric field at z=54 µm. The mode purity reduces as m increases.

4.4 Volumetric Imaging

Figure 4.9(a) shows a volumetric rendering of a Bessel beam with $m = 0$ and $\alpha = 3.9\,\mathrm{mrad}$ created with Eq. (4.33). This linearly polarized beam was created at $\lambda = 532\,\mathrm{nm}$ (Coherent Verdi 5W) using a phase-only spatial light modulator (SLM, Hamamatsu X10468-16) to imprint the phase of the field described by Eq. (4.33) on the collimated beam's wavefronts. The beam's intensity profile was measured by moving a standard video camera (NEC TI-324AII) along an optical rail in 2.5 mm increments over a range of one meter. Each transverse slice has a transverse spatial resolution of 8.64 µm. The transverse width of these beam's intensity maxima does not change appreciably over at least twice the plotted range.

Superpositions of Bessel beams can be obtained by superposing results of the form predicted by Eq. (4.34) [115]. These are particularly useful for projecting tractor beams. The field for an optical conveyor [103, 110, 111], for example, can be as simple as a two-fold superposition of equal-helicity Bessel beams:

$$E_{\alpha,m}^{\delta\alpha}(\boldsymbol{r}, \phi) = E_{\alpha,m}(\boldsymbol{r}) + e^{i\phi}\, E_{\alpha+\delta\alpha,m}(\boldsymbol{r}). \tag{4.35}$$

An example with $m = 0$, $\alpha = 3.9\,\mathrm{mrad}$ and $\delta\alpha = 4.9\,\mathrm{mrad}$ is presented in Fig. 4.5(c) and Fig. 4.9(b). This beam's axial intensity profile is characterized by a periodic array of maxima spaced by $\Delta z = \lambda[\tan(\alpha + \delta\alpha) - \tan\alpha]^{-1}$. The alternating intensity maxima and minima act as traps for illuminated objects that can be moved along the axis by varying the relative phase, ϕ [103, 110, 111].

Images were recorded with a total beam power of 1 mW, as recorded by an optical power meter (Coherent Lasermate). The upper limit of the conveyor

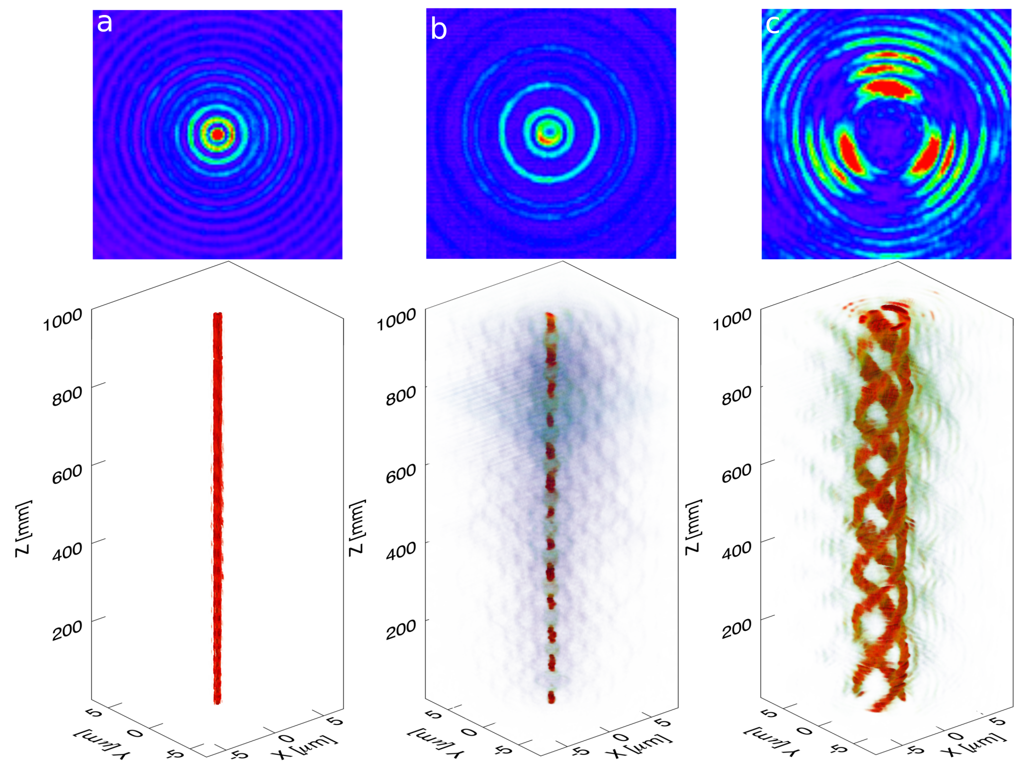

Fig. 4.9: Propagation-invariant modes projected with intermediate-plane holograms. (a) Bessel beam, $m = 0$, $\alpha = 3.9\,\mathrm{mrad}$. (b) Optical conveyor, $m = 0$, $\alpha_1 = 3.9\,\mathrm{mrad}$, $\alpha_2 = 8.8\,\mathrm{mrad}$. (c) Solenoidal tractor beam, $m_1 = -10$, $m_2 = -7$, $\alpha_1 = 6.4\,\mathrm{mrad}$, $\alpha_2 = 8.8\,\mathrm{mrad}$.

beam's power, 1 W, was set by the 3 W limit of the SLM, with a total diffraction efficiency of 0.3 into the desired mode. This represents a factor of 400 improvement of diffraction efficiency relative to a standard ring hologram [103, 110] given the SLM's 800×600 array of phase pixels. The beam's non-diffracting range exceeds that of previously reported holographically-projected conveyor modes [103, 110] by a factor of more than 10^3.

Intermediate-plane holography is particularly useful for projecting more sophisticated superpositions of Bessel beams, such as the solenoidal wave presented in Fig. 4.5(d) and Fig. 4.9(c). This two-beam superposition has the general form

$$E^{\mu}_{\alpha,m}(\boldsymbol{r}) = E_{\alpha,m}(\boldsymbol{r}) + \frac{J_m(j'_{m,2})}{J_{m'}(j'_{m',1})} E_{\alpha',m'}(\boldsymbol{r}), \tag{4.36}$$

where $m' = m + \mu$, $\sin\alpha' = (j'_{m,2}/j'_{m',1})\sin\alpha$, and $j'_{m,n}$ is the n-th zero of $J'_m(x)$. The particular realization in Fig. 4.9(c) is a three-fold ($\mu = 3$) tractor-beam mode [112] with $m = -10$ and $\alpha = 6.4\,\text{mrad}$. These parameters satisfy the condition $\cos(\alpha) > [m/(m+\mu)]\cos(\alpha+\delta\alpha)$ required for a solenoidal wave to act as a tractor beam [112]. As with the conveyor beam, the intermediate-plane hologram projecting the solenoidal tractor beam has a diffraction efficiency of roughly 0.3, and yields a non-diffracting range exceeding 1 m.

Solenoidal modes are examples of accelerating waves [116] in the sense that the position of the principal intensity maximum, is a non-linear function of axial position. Intermediate-plane holography therefore is useful for creating non-diffracting accelerating modes with high diffraction efficiency.

The same approach used for these demonstrations also can be applied to more complicated superpositions of Bessel modes [109, 117–119]. In all cases, the intermediate-plane approach should provide better mode purity, longer range and higher diffraction efficiency than conventional holographic mode-conversion techniques.

In addition to projecting collimated modes, intermediate-plane holograms can project waves that converge or diverge at a specified rate. This is achieved by deliberately mis-matching the placement of the intermediate plane with the back focal plane of the converging element. For intermediate-plane holograms with integrated converging phase profiles, this is achieved by having the displacement, z, differ from the focal length f. In that case, the resulting divergence angle is $\gamma = \tan^{-1}(1 - z/f)$. Each superposed mode in such an element, furthermore, can have a different divergence angle.

4.5 Conclusion

Intermediate-plane holography is particularly useful for projecting modes whose ideal Fresnel holograms are dominated by large amplitude variations, and so suffer from low diffraction efficiency. In addition to improving diffraction efficiency, shifting the hologram plane also can improve mode purity by moving the length scale for phase variations into the spatial bandwidth of a practical diffractive optical element. Both of these elements figure in the success of intermediate-plane holograms for projecting Bessel beams and their superpositions. Because Bessel beams are the natural basis for propagation-invariant modes, intermediate-plane holography lends itself naturally to long-range projection. We have demonstrated meter-scale projection using centimeter-scale optical elements. These same elements have additional potential applications for topologically multiplexing and demultiplexing non-diffracting modes for optical communications [105–107]. The same ability to project sophisticated superpositions of topological modes could have additional applications to remote sensing and LIDAR [120]. Finally, the same principals discussed here in the context of optical holography should apply equally well to other types of waves, most notably to acoustic waves.

4.6 Acknowledgment

This work was supported primarily by the National Science Foundation through Award no. DMR-1305875 and in part by NASA through Award no. NNX13AK76G and through the NASA Space Technology Research Fellowship (NSTRF) program under Award no. NNX15AQ40H.

Chapter 5

Classically accelerating solenoidal wave packets in two dimensions

5.1 Strongly Localized Solenoidal Beam

Our goal is to have an electric field of the form:

$$G(\mathbf{r}, z) = \delta(r - R)\delta(\theta - \theta_0(z))e^{i\phi(\mathbf{r},z)} \tag{5.1}$$

, where $\theta_0(z) = \frac{z}{\gamma}$. Here γ will define the pitch of the spiral. We also seek the Green's function to be of the form:

$$G(\mathbf{r}, z) = \Sigma_{n=0}^{\infty} a_n \psi_n(\mathbf{r}, z) \tag{5.2}$$

, where $\psi_n(\mathbf{r}, z)$ are given by:

$$\psi_n(\mathbf{r}, z) = A_n J_n(k_n r \cos\alpha_n) e^{in\theta} e^{ik_n z \cos\alpha_n} \tag{5.3}$$

, where A_n is a normalization constant. Using 2 forms of Green's function we obtain the coefficients a_n in Eq.5.2.

$$a_n = \frac{1}{A_n} R J_n(k_n R \sin\alpha_n) e^{-ik_n z \cos\alpha_n} e^{-in\frac{z}{\gamma}} e^{i\phi(R,z)} \tag{5.4}$$

We want the coefficients a_n to be z independent. Therefore,

$$\phi(R, z) = k_n z \cos\alpha_n + n\frac{z}{\gamma} \tag{5.5}$$

So the final Green's function is given by:

$$G(\mathbf{r}, z) = \Sigma_{n=0}^{\infty} J_n(k_n R \sin\alpha_n) J_n(k_n r \sin\alpha_n) e^{in\theta} e^{ik_n z \cos\alpha_n} \tag{5.6}$$

Say, $k_i = k_j = k = \frac{2\pi}{\lambda}$ and $\phi(R, z) = \phi_0 z$. Then

$$\cos\alpha_n = \frac{1}{k}(\phi_0 - \frac{n}{\gamma}) \tag{5.7}$$

5.2 QM

In 1979, Balazs and Berry reported the discovery of shape-preserving wave packets for quantum mechanical particles that translate with uniform acceleration in one dimension [121]. Taking the form of Airy functions, these wave packets appear to violate Ehrenfest's theorem because they accelerate in the absence of any applied force. This conundrum is resolved by recognizing that an Airy wave packet is not square-integrable and thus is best interpreted as an ensemble of non-accelerating single-particle plane-wave states [121, 122]. Optical analogs to Airy wave packets have been realized in holographically-patterned laser beams, the temporal evolution of the quantum state being modeled through the spatial evolution of the light's intensity profile [123–125]. In this case, the beam's intensity profile translates along a parabolic path as it propagates, without otherwise distorting. The analogy between the spatial structure of a propagating light beam and the temporal evolution of a quantum mechanical wave packet reflects the homology of the paraxial wave equation with Schrödinger's equation.

Here, we introduce an alternative class of shape-preserving wave packets in two dimensions that describe a particle undergoing uniform circular motion in the force-free region of a circular box. Although the confined wave packet's time evolution is consistent with Ehrenfest's theorem, the equivalent truncated wave packet in free space appears to accelerate in the absence of a central force. Rotating states also have the surprising property that the classical angular momentum they carry differs from their quantum mechanical angular momentum, and indeed can have the opposite sign. We illustrate these properties through experimental realizations of analogous propagation-invariant laser modes projected with intermediate-plane holography [126].

The wave function, $\Psi(\boldsymbol{r})$, of a nonrelativistic particle of mass m moving in a two-dimensional circular box of radius R can be expressed in polar coordinates, $\boldsymbol{r} = (r, \phi)$, in terms of eigenfunctions of the force-free time-independent

Schrödinger equation,

$$-\frac{\hbar^2}{2m}\,\nabla^2\Psi(\boldsymbol{r}) = E\,\Psi(\boldsymbol{r}), \tag{5.8a}$$

with polar Laplacian

$$\nabla^2 = \frac{\partial^2}{\partial r^2} + \frac{1}{r}\frac{\partial}{\partial r} + \frac{1}{r^2}\frac{\partial^2}{\partial \phi^2}, \tag{5.8b}$$

subject to the boundary condition

$$\Psi(R,\phi) = 0. \tag{5.8c}$$

Equation (5.8) is satisfied by the Bessel wave functions, $|n,\nu\rangle$, whose spatial representation is

$$\Psi_{n,\nu}(\boldsymbol{r}) = \langle \boldsymbol{r}|n,\nu\rangle \tag{5.9a}$$

$$= A_{n,\nu}\,J_n\left(j_{n,\nu}\frac{r}{R}\right)\,e^{in\phi}, \tag{5.9b}$$

where $J_n(x)$ is a Bessel function of the first kind of order n, and where $j_{n,\nu}$ is its ν-th zero. The prefactor

$$A_{n,\nu} = \left[\pi^{1/2} R\,J_{n+1}(j_{n,\nu})\right]^{-1} \tag{5.9c}$$

ensures that the corresponding probability density

$$\rho_{n,\nu}(\boldsymbol{r}) = \left|\Psi_{n,\nu}(\boldsymbol{r})\right|^2, \tag{5.10}$$

is properly normalized. The Bessel states then are orthonormal:

$$\langle n',\nu'|n,\nu\rangle = \delta_{n,n'}\delta_{\nu,\nu'}. \tag{5.11}$$

Their eigenenergies,

$$E_{n,\nu} = \frac{\hbar^2 j_{n,\nu}^2}{2mR^2}, \tag{5.12}$$

depend on both the azimuthal quantum number, n, and the radial quantum number, ν. The associated frequency, $\omega_{n,\nu} = E_{n,\nu}/\hbar$, establishes the eigenstates' time evolution,

$$\Psi_{n,\nu}(\boldsymbol{r}, t) = \langle \boldsymbol{r} | n, \nu \rangle \; e^{-i\omega_{n,\nu} t}. \tag{5.13}$$

The states described by Eqs. (5.9) and (5.13) are analogous to optical Bessel beams [5, 6], with the time in Eq. (5.13) serving as an analog to the light wave's axial coordinate. Like their optical counterparts, Bessel wavefunctions carry angular momentum with expectation value

$$\langle L_z \rangle = -i\hbar \int \Psi_{n,\nu}^*(\boldsymbol{r}) \frac{\partial}{\partial \phi} \Psi_{n,\nu}(\boldsymbol{r}) \, d^2 r = n\hbar \tag{5.14}$$

that depends on n, but not on ν. For optical Bessel beams, this orbital angular momentum is a classical property of the electromagnetic field [127, 128] that also is a quantum mechanical property of the individual photons [129]. For the particle in a circular box, it is strictly a quantum mechanical property. The particle's probability density, $\rho_{n,\nu}(\boldsymbol{r})$, is independent of time, which means that the particle is stationary in the classical sense and therefore carries no classical angular momentum. Similar discrepancies between the classical and quantum mechanical angular momentum have been noted for Landau states in free electron beams [130].

Although individual Bessel eigenmodes are time-invariant, some of their superpositions have probability densities that rotate at a uniform rate without otherwise distorting [109, 118, 131]. Some of these rotating wave packets consti-

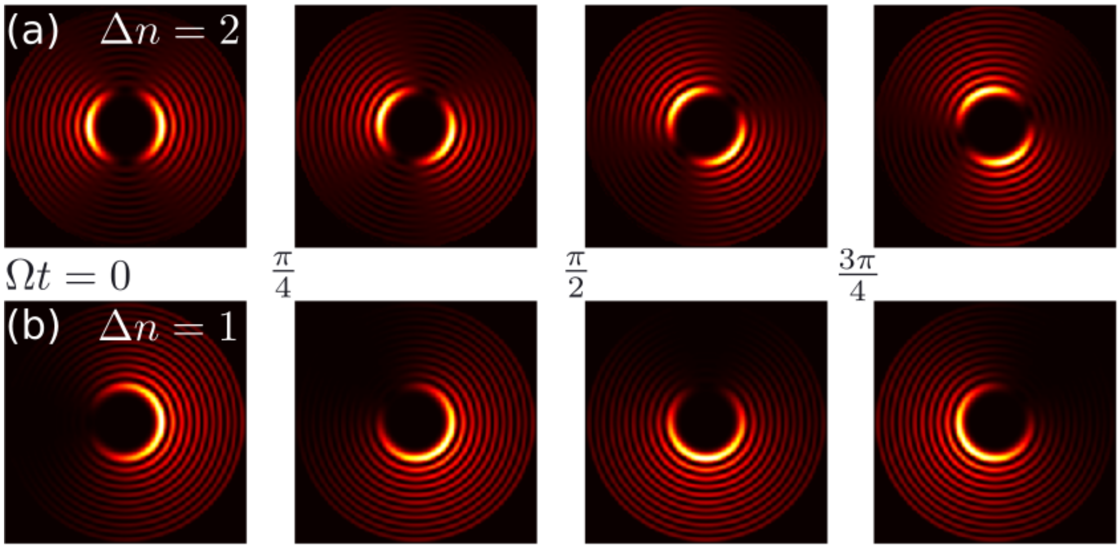

Fig. 5.1: Rotation of solenoidal states with $n = 6$, $\nu = 15$, and $\nu' = \nu - 1$. (a) Non-accelerating wave packet with $\Delta n = n' - n = 2$. (b) Accelerating state with $\Delta n = 1$.

tute accelerating states in the sense that the expectation value of the particle's position traces out an accelerating trajectory. These are not simply related to two-dimensional Airy states or to related Matthieu and Weber states [132] or to their generalizations [133–135], and thus constitute a distinct class of accelerating states in two dimensions.

Minimal examples of rotating wave packets can be constructed by superposing two Bessel states:

$$\Psi(\boldsymbol{r}, t) = \frac{1}{\sqrt{2}} \left[\Psi_{n,\nu}(\boldsymbol{r}, t) + \Psi_{n',\nu'}(\boldsymbol{r}, t)\right]. \tag{5.15}$$

For clarity, we arrange indices so that $\Delta n = n' - n > 0$. This superposition's probability density

$$\rho(\boldsymbol{r},t) = \frac{1}{2}\,[\rho_{n,\nu}(\boldsymbol{r}) + \rho_{n',\nu'}(\boldsymbol{r})] + \\ [\rho_{n,\nu}(\boldsymbol{r})\rho_{n',\nu'}(\boldsymbol{r})]^{1/2}\,\cos\left(\Delta n[\phi - \Omega t]\right), \quad (5.16)$$

rotates around the origin with an angular frequency

$$\Omega = \frac{\hbar}{2mR^2}\,\frac{j^2_{n',\nu'} - j^2_{n,\nu}}{\Delta n}. \quad (5.17)$$

Aside from this rotation, the state neither broadens nor otherwise distorts. The resulting periodic recurrence differs from the breathing modes identified in generalized Airy states [125]. Instead, it closely resembles the discrete propagation invariance of rotating optical modes [**?**], particularly solenoidal beams [109]. For this reason, we refer to the rotating wave functions described by Eq. (5.15) as solenoidal states. Figure 5.1 shows the time evolution of two illustrative examples.

Most solenoidal wave packets are not accelerating states in the sense identified by Balazs and Berry. Those with $\Delta n > 1$, such as the example in Fig. 5.1(a), are symmetric about the origin; the expectation value of the particle's position coincides with the center of the box. Classically, therefore, such states resemble their constituent Bessel states in that the particle remains motionless at the origin even as its probability density rotates.

Solenoidal states with $\Delta n = 1$ are asymmetric, as can be seen in Fig. 5.1(b). The expectation value for the particle's position,

$$\langle \boldsymbol{r}(t) \rangle = \alpha R\,[\cos(\Omega t)\,\hat{x} + \sin(\Omega t)\,\hat{y}], \quad (5.18)$$

undergoes uniform circulation motion at angular frequency Ω and radius $\langle r \rangle = \alpha R$, where

$$\alpha = \frac{\int_0^1 J_{n+1}(j_{n+1,\nu'} x)\, J_n(j_{n,\nu} x)\, x^2\, dx}{J_{n+2}(j_{n+1,\nu'})\, J_{n+1}(j_{n,\nu})} \tag{5.19a}$$

$$= \frac{2 j_{n+1,\nu'} j_{n,\nu}}{(j_{n+1,\nu'}^2 - j_{n,\nu}^2)^2}. \tag{5.19b}$$

This seems remarkable because no force acts on the particle within the box. Such force-free acceleration appears to violate Ehrenfest's theorem, which relates the expectation value of the particle's acceleration to the expectation value of the force acting on the particle,

$$\frac{d^2 \langle \boldsymbol{r}(t) \rangle}{dt^2} = \frac{1}{m} \langle \boldsymbol{F}(\boldsymbol{r}(t)) \rangle . \tag{5.20}$$

In the present case, $\boldsymbol{F}(\langle \boldsymbol{r}(t) \rangle) = 0$ in the force-free region within the box, but

$$\frac{d^2 \langle \boldsymbol{r}(t) \rangle}{dt^2} = -\alpha R\, \Omega^2 \hat{r}. \tag{5.21}$$

The apparent discrepancy can be explained because $\boldsymbol{F}(\langle \boldsymbol{r}(t) \rangle) \neq \langle \boldsymbol{F}(\boldsymbol{r}(t)) \rangle$.

The integrability of the solenoidal wave packets comes at the cost of applying the boundary condition from Eq. (5.8c) at $r = R$. The confined particle exerts a pressure on the wall,

$$P = -\frac{1}{2\pi R} \frac{dE}{dR} \tag{5.22a}$$

$$= \frac{\hbar^2}{4\pi m R^4} \left(j_{n+1,\nu'}^2 + j_{n,\nu}^2 \right) . \tag{5.22b}$$

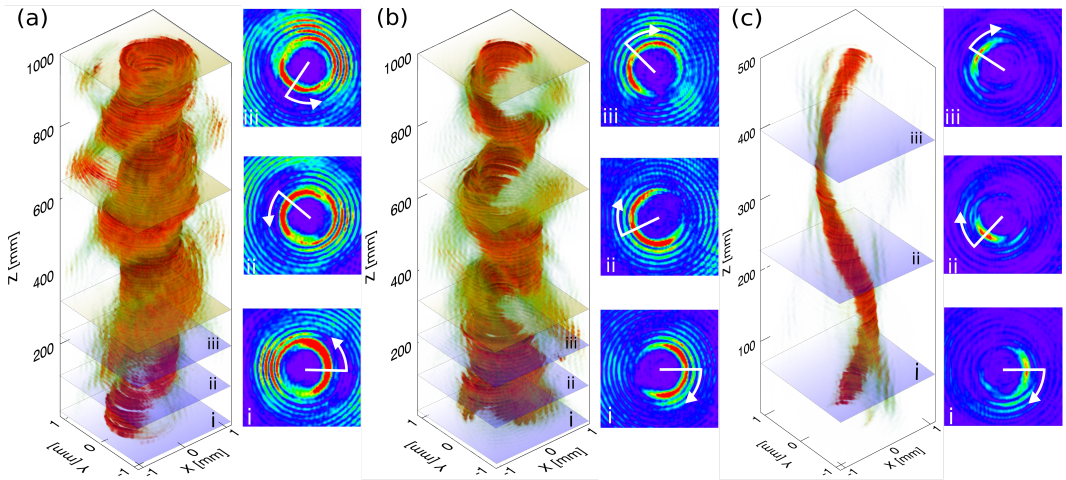

Fig. 5.2: Optical realization of accelerating solenoidal states. Volumetric reconstructions of asymmetric solenoidal waves described by Eq. (5.15) with $\Delta n = 1$. (a) Positive helicity: $n = 20$, $\nu = 15$, $\nu' = 14$. (b) Negative helicity: $\nu = 14$, $\nu' = 15$. (c) Four-mode ($n = 10, 11, 12, 13$) superposition yielding improved in-plane localization.

By Newton's third law, the wall exerts a complementary force on the wave packet that is directed radially inward. When averaged over angles, the net force acting on the particle located at $\langle \boldsymbol{r} \rangle$ is

$$\langle \boldsymbol{F}(\boldsymbol{r}) \rangle = -\beta R\, P\, \hat{r}, \tag{5.23a}$$

where

$$\beta = \lim_{\epsilon \to 0} \frac{\int_0^{2\pi} \rho(\boldsymbol{r}, t) \cos(\phi - \Omega t)\, d\phi \Big|_{r=R-\epsilon}}{\int_0^{2\pi} \rho(\boldsymbol{r}, t)\, d\phi \Big|_{r=R-\epsilon}} \tag{5.23b}$$

$$= \frac{2 j_{n+1,\nu'} j_{n,\nu}}{j_{n+1,\nu'}^2 + j_{n,\nu}^2}. \tag{5.23c}$$

Comparison with Eq. (5.21) confirms that Ehrenfest's theorem is satisfied: the force responsible for the particle's classical circular motion is exerted by the wave function's interaction with the bounding wall.

In principle, accelerating solenoidal states can be prepared as superpositions of Bessel beams without confining boundary conditions. Such unconfined states rotate without a central force, and so appear to violate Ehrenfest's theorem. Because Bessel states are not square-integrable, however, they are best interpreted as superpositions of plane-wave states [121]. The rotation of solenoidal wave packets then represents the ensemble-averaged behavior of multiple particles' non-accelerating trajectories.

The possibility of Ehrenfest violations arises again for normalizable approximations to unconfined solenoidal wave packets that are prepared by truncating $\Psi(\boldsymbol{r}, t)$ at $r = R$. These truncated wave packets still appear to rotate, and they evolve under truly force-free conditions. To illustrate this phenomenon, Fig. 5.2 presents optical analogs of truncated solenoidal states. We prepare these solenoidal beams of light by using intermediate-plane holograms [126] to convert the linearly polarized Gaussian TEM_{00} beam from a solid state laser (Coherent Verdi 5W) into a superposition of helical Bessel modes of the form described by Eq. (5.15). The mode-converting holograms are imprinted on the beam with a phase-only liquid crystal spatial light modulator (Hamamatsu X10468-16).

Figure 5.2(a) and Fig. 5.2(b) show volumetric reconstructions of two solenoidal laser beams with $\Delta n = 1$. The data for these reconstructions were obtained by translating a video camera (NEC TI-324AII) along the optical axis and combining the resulting stack of images. Each reconstruction shows three complete cycles of shape-preserving propagation. The solenoid in Fig. 5.2(a) has a right-handed twist while that in Fig. 5.2(b) is left-handed. Each volumetric reconstruction is paired with three transverse slices from the planes labeled (i), (ii) and (iii) in the renderings. These slices show three stages in the intensity distributions' rotation about the optical axis at 120° intervals. Additional planes in the renderings correspond to each of the three complete rotations captured over the course of 1 m of propagation. The full non-diffracting range of these beams extends beyond 2 m.

The two-state superpositions discussed so far are not the only accelerating wave packets. Figure 5.2(c) shows a four-state superposition designed to optimally localize the wave packet as it spirals around the origin. In this case, there can be no doubt that the point of maximum intensity rotates about the optical axis, and therefore that the most probable particle position, $\boldsymbol{r}^*(t)$, undergoes uniform circular motion under force-free conditions.

Figure 5.3(a) shows a representative simulation of $\boldsymbol{r}^*(t)$ superimposed on a snapshot of the initial distribution, $\rho(\boldsymbol{r}, 0)$. Figure 5.3(b) shows the corresponding experimental measurement of $\boldsymbol{r}^*(z)$. The angular position of the peak, $\theta^*(t)$, advances uniformly, as can be seen in Fig. 5.3(c). For clarity, we have scaled the simulation time to best superimpose the temporal evolution of the simulation data on the spatial evolution of the experimental data, $\theta^*(z)$.

This apparent contradiction of the Ehrenfest theorem is resolved by tracking the mean particle position, $\langle \boldsymbol{r}(t) \rangle$, which also is plotted in Fig. 5.3. Results for $\langle x(t) \rangle$ and $\langle x(z) \rangle$ are plotted in Fig. 5.3(d), with the simulation time again scaled as in Fig. 5.3(c). In both simulation and experiment, the classical trajectory of the unconfined rotating wave packet actually *translates* steadily away from the beam's axis with an impact parameter, b set by the average position at $t = 0$. This motion arises because the truncated wave packet diffracts beyond $r = R$ by precisely the amount needed to conserve momentum under force-free conditions. The nature of the state's time evolution is masked because diffraction has little apparent influence on the wave packet's structure at early times, particularly near the center of the system. Remarkably, this means that the finite-aperture solenoidal laser modes presented in Fig. 5.2 are not accelerating states in the sense introduced by Balasz and Berry, despite their apparent rotation.

Although the confined particle's classical acceleration can be accounted for by the influence of boundary conditions, its rate of circulation is less straightforward to interpret. The classical angular momentum carried by an accelerating solenoidal wave packet is

$$L_z^{(c)} = m\alpha^2 R^2 \Omega \tag{5.24a}$$

$$= 2\frac{j_{n+1,\nu'}^2 j_{n,\nu}^2}{(j_{n+1,\nu'}^2 - j_{n,\nu}^2)^3}\,\hbar, \tag{5.24b}$$

which differs from the state's quantum mechanical angular momentum,

$$\langle L_z \rangle = \left(n + \frac{1}{2}\right)\hbar. \tag{5.25}$$

Indeed, $L_z^{(c)}$ and $\langle L_z \rangle$ can have opposite signs depending on the choice of radial quantum numbers ν and ν'. The solenoidal states represented in Figs. 5.2(a) and 5.2(b), for example, have opposite classical angular momentum even though they carry the same quantum mechanical angular momentum. Unconfined solenoidal

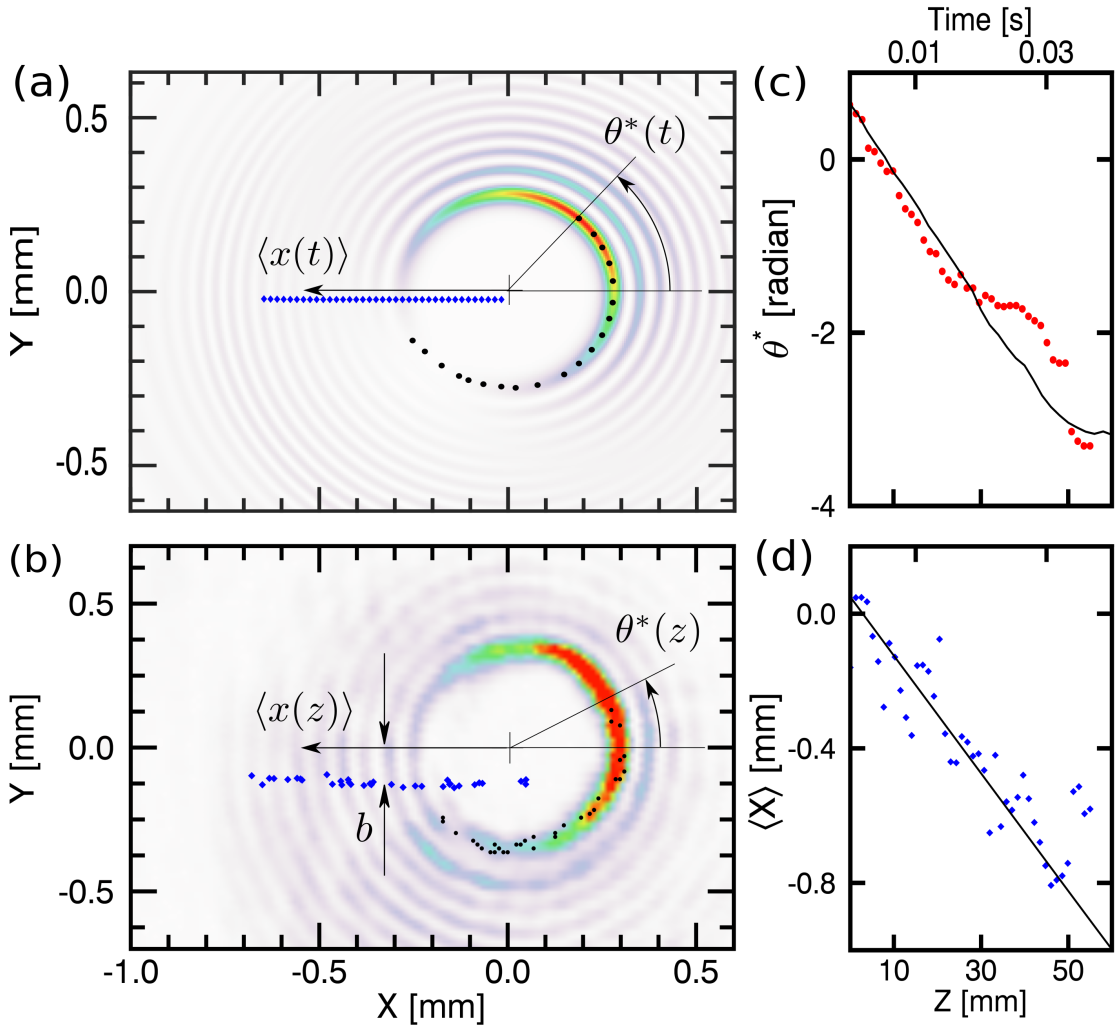

Fig. 5.3: Translation of a rotating wave packet. (a) Simulation of an accelerating state with $n = 20$, $\nu = 16$ and $\nu' = 17$. The image shows a region of interest around the center of the probability density $\rho(\boldsymbol{r}, t)$. Discrete points show the time evolution of the the most probable position $\boldsymbol{r}^*(t)$, which circulates, and of the expectation value of the position $\langle \boldsymbol{r}(t) \rangle$, which translates. (b) Corresponding experimental realization. (c) Time evolution of the mode position $\theta^*(t)$ in the simulation (solid curve) compared with $\theta^*(z)$ from the experimental data (discrete points). (d) Time evolution of the simulated wave packet's mean position $\langle x(t) \rangle$ compared with the position of the experimental center of brightness, $\langle x(z) \rangle$.

states also carry classical angular momentum

$$L_z^{(c)} = m \left[\langle \boldsymbol{r}(0) \rangle \times \frac{d \langle \boldsymbol{r}(t) \rangle}{dt} \right] \cdot \hat{z} \tag{5.26}$$

that is equal to the confined value from Eq. (5.24) and generally differs from the quantum-mechanical value, Eq. (5.25). Similar discrepancies between classical and quantum mechanical angular momenta have been been observed in the spatial structure of holographically-patterned electron beams [130]. A comprehensive paradigm for understanding these discrepancies and their physical consequences remains elusive.

5.3 Acknowledgment

This work was supported primarily by the National Science Foundation under award number DMR-1305875 and in part by the MRSEC program of the NSF through award number DMR-1420073. The authors are grateful for helpful conversations with David Pine, Paul Chaikin and Aaron Yevick.

Chapter 6

Conclusions

Bibliography

[1] Alison M. Yao and Miles J. Padgett, "Orbital angular momentum: origins, behavior and applications," Adv. Opt. Photon. **3**, 161–204 (2011).

[2] Richard A. Beth, "Mechanical detection and measurement of the angular momentum of light," Phys. Rev. **50**, 115–125 (1936).

[3] Sang-Hyuk Lee, Yohai Roichman, and David G. Grier, "Optical solenoid beams," Opt. Express **18**, 6988–6993 (2010).

[4] M. V. Berry and N. L. Balazs, "Nonspreading wave packets," American Journal of Physics **47**, 264–267 (1979), https://doi.org/10.1119/1.11855 .

[5] J. Durnin, "Exact-solutions for nondiffracting beams. 1. the scalar theory," J. Opt. Soc. Am. A **4**, 651–654 (1987).

[6] J. Durnin, J. J. Miceli, Jr, and J. H. Eberly, "Diffraction-free beams," Phys. Rev. Lett. **58**, 1499–1501 (1987).

[7] Brian Vohnsen, "A short history of optics," Physica Scripta **T109**, 75 (2004).

[8] G. Abetti, "Ronchi v. the nature of light," Scientia, Rivista di Scienza **65**, 719 (1971).

[9] FixQuotes.com, “Pythagoras the mathematician, biography, facts and quotes,” .

[10] Atomic Model Timeline, “Democritus,” .

[11] History-biography, “Empedocles,” (2019).

[12] J. C. Maxwell, “Li. on physical lines of force,” The London, Edinburgh, and Dublin Philosophical Magazine and Journal of Science **21**, 338–348 (1861).

[13] James Clerk Maxwell, “VIII. A dynamical theory of the electromagnetic field,” Philosophical transactions of the Royal Society of London **155**, 459–512 (1865).

[14] Salvo D’Agostino, “Hertz’s researches on electromagnetic waves,” Historical Studies in the Physical Sciences **6**, 261–323 (1975).

[15] John David Jackson, *Classical electrodynamics*, 3rd ed. (Wiley, New York, NY, 1999).

[16] J.W. Goodman, *Introduction to Fourier Optics*, 2nd ed. (MaGraw-Hill, 1996).

[17] E. Hecht, *Optics*, 4th ed. (Addison-Wesley, 1998).

[18] M Born and E Wolf, *Principles of Optics*, 7th ed. (Cambridge University Press, 1999).

[19] Sang-Hyuk Lee and David G. Grier, “Holographic microscopy of holographically trapped three-dimensional structures,” Opt. Express **15**, 1505–1512 (2007).

[20] G. Kirchhoff, "Zur theorie der lichtstrahlen," Annalen der Physik **254**, 663–695 (1883).

[21] Robert L Lucke, "Rayleigh–sommerfeld diffraction and poisson's spot," European Journal of Physics **27**, 193–204 (2006).

[22] John C. Heurtley, "Scalar rayleigh–sommerfeld and kirchhoff diffraction integrals: A comparison of exact evaluations for axial points∗," J. Opt. Soc. Am. **63**, 1003–1008 (1973).

[23] Arnold Sommerfeld, *Optics*, Lectures on Theoretical Physics, Vol. IV (1954) pp. xiii + 383, translated by Otto Laporte and P. A. Moldauer.

[24] Wikipedia, "Johannes kepler," (2019).

[25] Wikipedia, "Halley's comet," (2019).

[26] P. C. Chaumet and M. Nieto-Vesperinas, "Time-averaged total force on a dipolar sphere in an electromagnetic field," Opt. Lett. **25**, 1065–1067 (2000).

[27] James P. Gordon, "Radiation forces and momenta in dielectric media," Phys. Rev. A **8**, 14–21 (1973).

[28] Clifton E. Dungey and Craig F. Bohren, "Light scattering by nonspherical particles: a refinement to the coupled-dipole method," J. Opt. Soc. Am. A **8**, 81–87 (1991).

[29] B. T. Draine and Jeremy Goodman, "Beyond Clausius-Mossotti: Wave Propagation on a Polarizable Point Lattice and the Discrete Dipole Approximation," Astrophysical Journal **405**, 685 (1993).

[30] A. Ashkin, J. M. Dziedzic, J. E. Bjorkholm, and Steven Chu, "Observation of a single-beam gradient force optical trap for dielectric particles," Opt. Lett. **11**, 288–290 (1986).

[31] Wolfram MathWorld, "Topology," .

[32] Daniel Leykam and Y. D. Chong, "Edge solitons in nonlinear-photonic topological insulators," Phys. Rev. Lett. **117**, 143901 (2016).

[33] Xin Zhou, You Wang, Daniel Leykam, and Y D Chong, "Optical isolation with nonlinear topological photonics," New Journal of Physics **19**, 095002 (2017).

[34] Sabyasachi Barik, Aziz Karasahin, Christopher Flower, Tao Cai, Hirokazu Miyake, Wade DeGottardi, Mohammad Hafezi, and Edo Waks, "A topological quantum optics interface," Science **359**, 666–668 (2018), https://science.sciencemag.org/content/359/6376/666.full.pdf .

[35] D. Hsieh, D. Qian, L. Wray, Y. Xia, Y. S. Hor, R. J. Cava, and M. Z. Hasan, "A topological dirac insulator in a quantum spin hall phase," Nature **452**, 970 EP – (2008).

[36] F. Duncan M. Haldane, "Nobel lecture: Topological quantum matter," Rev. Mod. Phys. **89**, 040502 (2017).

[37] Tomoki Ozawa, Hannah M. Price, Alberto Amo, Nathan Goldman, Mohammad Hafezi, Ling Lu, Mikael C. Rechtsman, David Schuster, Jonathan Simon, Oded Zilberberg, and Iacopo Carusotto, "Topological photonics," Rev. Mod. Phys. **91**, 015006 (2019).

[38] Roarke Horstmeyer, Benjamin Judkewitz, Ivo M. Vellekoop, Sid Assawaworrarit, and Changhuei Yang, "Physical key-protected one-time pad," Scientific Reports **3**, 3543 EP – (2013).

[39] R. Horstmeyer, B. Judkewitz, I. Vellekoop, and C. Yang, "Secure storage of cryptographic keys within random volumetric materials," in *CLEO: 2013* (2013) pp. 1–5.

[40] Ying Min Wang, Benjamin Judkewitz, Charles A. DiMarzio, and Changhuei Yang, "Deep-tissue focal fluorescence imaging with digitally time-reversed ultrasound-encoded light," Nature Communications **3**, 928 EP – (2012).

[41] Ioannis N. Papadopoulos, Salma Farahi, Christophe Moser, and Demetri Psaltis, "Focusing and scanning light through a multimode optical fiber using digital phase conjugation," Opt. Express **20**, 10583–10590 (2012).

[42] V.Yu. Bazhenov, M.S. Soskin, and M.V. Vasnetsov, "Screw dislocations in light wavefronts," Journal of Modern Optics **39**, 985–990 (1992), https://doi.org/10.1080/09500349214551011 .

[43] Jennifer E. Curtis and David G. Grier, "Modulated optical vortices," Opt. Lett. **28**, 872–874 (2003).

[44] David G. Grier, "A revolution in optical manipulation," Nature **424**, 810–816 (2003).

[45] John Frederick Nye and Michael Victor Berry, "Dislocations in wave trains," .

[46] M.W. Beijersbergen, R.P.C. Coerwinkel, M. Kristensen, and J.P. Woerdman, "Helical-wavefront laser beams produced with a spiral phaseplate," Optics Communications **112**, 321 – 327 (1994).

[47] Jonathan Leach, Mark R. Dennis, Johannes Courtial, and Miles J. Padgett, "Knotted threads of darkness," Nature **432**, 165–165 (2004).

[48] Fred M. Dickey, "Laser beam shaping," Opt. Photon. News **14**, 30–35 (2003).

[49] J.-L. Beuzit, L. Demailly, E. Gendron, P. Gigan, F. Lacombe, D. Rouan, N. Hubin, D. Bonaccini, E. Prieto, F. Chazallet, D. Rabaud, P.-Y. Madec, G. Rousset, R. Hofmann, and F. Eisenhauer, "Adaptive optics on a 3.6-meter telescope. the adonis system." Experimental Astronomy **7**, 285–292 (1997).

[50] J. L. Beuzit, P. Thebault, G. Perrin, and D. Rouan, "Adaptative optics imaging of the Frosty Leo nebula." "Astronomy and Astrophysics" **291**, L1–L4 (1994).

[51] Anna T O'Neil and Miles J Padgett, "Three-dimensional optical confinement of micron-sized metal particles and the decoupling of the spin and orbital angular momentum within an optical spanner," Optics Communications **185**, 139 – 143 (2000).

[52] Simon Parkin, Gregor Knüner, Timo A. Nieminen, Norman R. Heckenberg, and Halina Rubinsztein-Dunlop, "Measurement of the total optical angular momentum transfer in optical tweezers," Opt. Express **14**, 6963–6970 (2006).

[53] V. Garcés-Chávez, D. McGloin, M. J. Padgett, W. Dultz, H. Schmitzer, and K. Dholakia, "Observation of the transfer of the local angular momentum

density of a multiringed light beam to an optically trapped particle," Phys. Rev. Lett. **91**, 093602 (2003).

[54] Timo A. Nieminen, Simon Parkin, Theodor Asavei, Vincent L.Y. Loke, Norman R. Heckenberg, and Halina Rubinsztein-Dunlop, "Chapter 8 - optical vortex trapping and the dynamics of particle rotation," in *Structured Light and Its Applications*, edited by DAVID L. ANDREWS (Academic Press, Burlington, 2008) pp. 195 – 236.

[55] Graham Gibson, Johannes Courtial, Miles J. Padgett, Mikhail Vasnetsov, Valeriy Pas'ko, Stephen M. Barnett, and Sonja Franke-Arnold, "Free-space information transfer using light beams carrying orbital angular momentum," Opt. Express **12**, 5448–5456 (2004).

[56] Alan E Willner, Guodong Xie, Long Li, Yongxiong Ren, Yan Yan, Nisar Ahmed, Zhe Zhao, Zhe Wang, Cong Liu, Asher J Willner, Nima Ashrafi, Solyman Ashrafi, Moshe Tur, and Andreas F Molisch, "Design challenges and guidelines for free-space optical communication links using orbital-angular-momentum multiplexing of multiple beams," Journal of Optics **18**, 074014 (2016).

[57] Nenad Bozinovic, Yang Yue, Yongxiong Ren, Moshe Tur, Poul Kristensen, Hao Huang, Alan E. Willner, and Siddharth Ramachandran, "Terabit-scale orbital angular momentum mode division multiplexing in fibers," Science **340**, 1545–1548 (2013), https://science.sciencemag.org/content/340/6140/1545.full.pdf .

[58] Wei Shao, Sujuan Huang, Xianpeng Liu, and Musheng Chen, "Free-space

optical communication with perfect optical vortex beams multiplexing," Optics Communications **427**, 545 – 550 (2018).

[59] P. C. Maurer, J. R. Maze, P. L. Stanwix, L. Jiang, A. V. Gorshkov, A. A. Zibrov, B. Harke, J. S. Hodges, A. S. Zibrov, A. Yacoby, D. Twitchen, S. W. Hell, R. L. Walsworth, and M. D. Lukin, "Far-field optical imaging and manipulation of individual spins with nanoscale resolution," Nature Physics **6**, 912 EP – (2010).

[60] Milton Abramowitz and Irene A. Stegun, *Handbook of Mathematical Functions with Formulas, Graphs, and Mathematical Tables*, ninth dover printing, tenth gpo printing ed. (Dover, New York, 1964).

[61] L. Allen, M. W. Beijersbergen, R. J. C. Spreeuw, and J. P. Woerdman, "Orbital angular momentum of light and the transformation of laguerre-gaussian laser modes," Phys. Rev. A **45**, 8185–8189 (1992).

[62] G. Ruffato, M. Massari, and F. Romanato, "Generation of high-order laguerre–gaussian modes by means of spiral phase plates," Opt. Lett. **39**, 5094–5097 (2014).

[63] Jari Turunen and Ari T. Friberg, "Chapter 1 - propagation-invariant optical fields," (Elsevier, 2010) pp. 1 – 88.

[64] Zden**e**K Bouchal, Richard Horák, and Jaroslav Wagner, "Propagation-invariant electromagnetic fields: Theory and experiment," Journal of Modern Optics **43**, 1905–1920 (1996), https://doi.org/10.1080/09500349608232859 .

[65] Rafael Piestun and Joseph Shamir, "Generalized propagation-invariant wave fields," J. Opt. Soc. Am. A **15**, 3039–3044 (1998).

[66] J. Durnin, "Exact solutions for nondiffracting beams. i. the scalar theory," J. Opt. Soc. Am. A **4**, 651–654 (1987).

[67] D McGloin and K Dholakia, "Bessel beams: Diffraction in a new light," Contemporary Physics **46**, 15–28 (2005), https://doi.org/10.1080/0010751042000275259 .

[68] J. C. Gutiérrez-Vega, M. D. Iturbe-Castillo, and S. Chávez-Cerda, "Alternative formulation for invariant optical fields: Mathieu beams," Opt. Lett. **25**, 1493–1495 (2000).

[69] Miguel A Bandres and B M Rodríguez-Lara, "Nondiffracting accelerating waves: Weber waves and parabolic momentum," New Journal of Physics **15**, 013054 (2013).

[70] "The nobel prize in physics 2018(arthur ashkin - facts)," Nobel Media (2019).

[71] Alexander Rohrbach and Ernst H. K. Stelzer, "Trapping forces, force constants, and potential depths for dielectric spheres in the presence of spherical aberrations," Appl. Opt. **41**, 2494–2507 (2002).

[72] K Svoboda and S M Block, "Biological applications of optical forces," Annual Review of Biophysics and Biomolecular Structure **23**, 247–285 (1994), pMID: 7919782.

[73] Rustem I. Litvinov, Henry Shuman, Joel S. Bennett, and John W. Weisel, "Binding strength and activation state of single fibrinogen-integrin pairs on living cells," Proceedings of the National Academy of Sciences **99**, 7426–7431 (2002).

[74] G. J. Brouhard, H. T. Schek, and A. J. Hunt, "Advanced optical tweezers for the study of cellular and molecular biomechanics," IEEE Transactions on Biomedical Engineering **50**, 121–125 (2003).

[75] K Svoboda, P P Mitra, and S M Block, "Fluctuation analysis of motor protein movement and single enzyme kinetics," Proceedings of the National Academy of Sciences **91**, 11782–11786 (1994).

[76] Argha Mondal, Bryan Black, Young-tae Kim, and Samarendra Mohanty, "Loop formation and self-fasciculation of cortical axon using photonic guidance at long working distance," Scientific Reports **4**, 6902 EP – (2014).

[77] John C. Crocker and David G. Grier, "Microscopic measurement of the pair interaction potential of charge-stabilized colloid," Phys. Rev. Lett. **73**, 352–355 (1994).

[78] Sang-Hyuk Lee, Yohai Roichman, Gi-Ra Yi, Shin-Hyun Kim, Seung-Man Yang, Alfons van Blaaderen, Peter van Oostrum, and David G. Grier, "Characterizing and tracking single colloidal particles with video holographic microscopy," Opt. Express **15**, 18275–18282 (2007).

[79] F. C. Cheong, K. Xiao, and D. G. Grier, "¡em¿technical note:¡/em¿ characterizing individual milk fat globules with holographic video microscopy," *Journal of Dairy Science*, Journal of Dairy Science **92**, 95–99 (2009).

[80] Ke Xiao and David G. Grier, "Sorting colloidal particles into multiple channels with optical forces: Prismatic optical fractionation," Phys. Rev. E **82**, 051407 (2010).

[81] Chen Wang, Hagay Shpaisman, Andrew D. Hollingsworth, and David G. Grier, "Celebrating soft matter's 10th anniversary: Monitoring colloidal growth with holographic microscopy," Soft Matter **11**, 1062–1066 (2015).

[82] Chen Wang, Xiao Zhong, David B. Ruffner, Alexandra Stutt, Laura A. Philips, Michael D. Ward, and David G. Grier, "Holographic characterization of protein aggregates," *Journal of Pharmaceutical Sciences*, Journal of Pharmaceutical Sciences **105**, 1074–1085 (2016).

[83] Yasunori Igasaki, Fanghong Li, Narihiro Yoshida, Haruyoshi Toyoda, Takashi Inoue, Naohisa Mukohzaka, Yuji Kobayashi, and Tsutomu Hara, "High efficiency electrically-addressable phase-only spatial light modulator," Optical Review **6**, 339–344 (1999).

[84] H. He, N.R. Heckenberg, and H. Rubinsztein-Dunlop, "Optical particle trapping with higher-order doughnut beams produced using high efficiency computer generated holograms," Journal of Modern Optics **42**, 217–223 (1995).

[85] Eric R. Dufresne, Gabriel C. Spalding, Matthew T. Dearing, Steven A. Sheets, and David G. Grier, "Computer-generated holographic optical tweezer arrays," Review of Scientific Instruments **72**, 1810–1816 (2001).

[86] Jennifer E. Curtis, Brian A. Koss, and David G. Grier, "Dynamic holographic optical tweezers," Optics Communications **207**, 169 – 175 (2002).

[87] David G. Grier and Yael Roichman, "Holographic optical trapping," Appl. Opt. **45**, 880–887 (2006).

[88] Marco Polin, Kosta Ladavac, Sang-Hyuk Lee, Yael Roichman, and David G.

Grier, “Optimized holographic optical traps,” Opt. Express **13**, 5831–5845 (2005).

[89] Taro Ando, Yoshiyuki Ohtake, Naoya Matsumoto, Takashi Inoue, and Norihiro Fukuchi, “Mode purities of laguerre–gaussian beams generated via complex-amplitudemodulation using phase-only spatial light modulators,” Opt. Lett. **34**, 34–36 (2009).

[90] Vincent Bagnoud and Jonathan D. Zuegel, “Independent phase and amplitude control of a laser beam by use of a single-phase-only spatial light modulator,” Opt. Lett. **29**, 295–297 (2004).

[91] Lewis Z. Liu, Kevin O’Keeffe, David T. Lloyd, and Simon M. Hooker, “General analytic solution for far-field phase and amplitude control, with a phase-only spatial light modulator,” Opt. Lett. **39**, 2137–2140 (2014).

[92] Jesse W. Wilson, Philip Schlup, and Randy A. Bartels, “Ultrafast phase and amplitude pulse shaping with a single, one-dimensional, high-resolution phase mask.” Opt. Express **15**, 8979–8987 (2007).

[93] E. G. van Putten, I. M. Vellekoop, and A. P. Mosk, “Spatial amplitude and phase modulation using commercial twisted nematic lcds,” Appl. Opt. **47**, 2076–2081 (2008).

[94] Long Zhu and Jian Wang, “Arbitrary manipulation of spatial amplitude and phase using phase-only spatial light modulators,” Scientific Reports **4**, 7441 EP – (2014).

[95] Steven M. Block, “Making light work with optical tweezers,” Nature **360**, 493–495 (1992).

[96] Tomás Cizmár, Veneranda Garcés-Chávez, Kishan Dholakia, and Pavel Zemánek, "Optical conveyor belt for delivery of submicron objects," Applied Physics Letters **86**, 174101 (2005), https://doi.org/10.1063/1.1915543 .

[97] David B. Ruffner and David G. Grier, "Optical conveyors: A class of active tractor beams," Phys. Rev. Lett. **109**, 163903 (2012).

[98] David B. Ruffner and David G. Grier, "Universal, strong and long-ranged trapping by optical conveyors," Opt. Express **22**, 26834–26843 (2014).

[99] Sang-Hyuk Lee, Yohai Roichman, and David G. Grier, "Optical solenoid beams," Opt. Express **18**, 6988–6993 (2010).

[100] Jani Tervo and Jari Turunen, "Rotating scale-invariant electromagnetic fields," Opt. Express **9**, 9–15 (2001).

[101] Joseph W. Goodman, *Introduction to Fourier Optics*, 3rd ed. (McGraw-Hill, New York, 2005).

[102] Yohai Roichman and David G. Grier, "Projecting extended optical traps with shape-phase holography," Opt. Lett. **31**, 1675–1677 (2006).

[103] David B. Ruffner and David G. Grier, "Optical conveyors: A class of active tractor beams," Phys. Rev. Lett. **109**, 163903 (2012).

[104] David G. Grier, "A revolution in optical manipulation," Nature **424**, 810–816 (2003).

[105] Graham Gibson, Johannes Courtial, Miles J Padgett, Mikhail Vasnetsov, Valeriy Paśko, Stephen M Barnett, and Sonja Franke-Arnold, "Free-space

information transfer using light beams carrying orbital angular momentum," Opt. Express **12**, 5448–5456 (2004).

[106] Nenad Bozinovic, Yang Yue, Yongxiong Ren, Moshe Tur, Poul Kristensen, Hao Huang, Alan E Willner, and Siddharth Ramachandran, "Terabit-scale orbital angular momentum mode division multiplexing in fibers," Science **340**, 1545–1548 (2013).

[107] Alan E Willner, Hao Huang, Yan Yan, Yongxiong Ren, Nisar Ahmed, Goudong Xie, Changjing Bao, L Li, Y Cao, Z Zhao, J Wang, M P J Lavery, M Tur, S Ramachandran, A F Molisch, N Ashrafi, and S others Ashrafi, "Optical communications using orbital angular momentum beams," Advances in Optics and Photonics **7**, 66–106 (2015).

[108] Philip L. Marston, "Axial radiation force of a Bessel beam on a sphere and direction reversal of the force," J. Acoust. Soc. Am. **120**, 3518–3524 (2006).

[109] Sang-Hyuk Lee, Yohai Roichman, and David G. Grier, "Optical solenoid beams," Opt. Express **18**, 6988–6993 (2010).

[110] David B. Ruffner and David G. Grier, "Universal, strong and long-ranged trapping by optical conveyors," Opt. Express **22**, 26834–26853 (2014).

[111] Tomá**s Ciz**mar, Veneranda Garcés-Chávez, Kishan Dhokalia, and Pavel Zemánek, "Optical conveyor belt for delivery of submicron objects," Appl. Phys. Lett. **86**, 174101 (2005).

[112] Aaron Yevick, David B. Ruffner, and David G. Grier, "Tractor beams in the Rayleigh limit," Phys. Rev. A **93**, 043807 (2016).

[113] Max Born and Emil Wolf, *Principles of Optics*, 7th ed. (Cambridge University Press, Cambridge, 1999).

[114] Oto Brzobohatý, Tomás **Ciz**már, and Pavel Zemánek, "High quality quasi-Bessel beam generated by round-tip axicon," Opt. Express **16**, 12688–12700 (2008).

[115] D. McGloin, V. Garcés-Chávez, and K. Dholakia, "Interfering Bessel beams for optical micromanipulation," Opt. Lett. **28**, 657–659 (2003).

[116] M. V. Berry and N. L. Balazs, "Nonspreading wave packets," Am. J. Phys. **47**, 264–267 (1979).

[117] Tomás **Ciz**már and Kishan Dholakia, "Tunable Bessel light modes: engineering the axial propagation," Opt. Express **17**, 15558–15570 (2009).

[118] Ruslan Vasilyeu, Angela Dudley, Nikolai Khilo, and Andrew Forbes, "Generating superpositions of higher-order Bessel beams," Opt. Express **17**, 23389–23395 (2009).

[119] Igor A. Litvin, Angela Dudley, and Andrew Forbes, "Poynting vector and orbital angular momentum density of superpositions of Bessel beams," Opt. Express **19**, 16760–16771 (2011).

[120] Neda Cvijetic, Giovanni Milione, Ezra Ip, and Ting Wang, "Detecting lateral motion using light's orbital angular momentum," Sci. Rep. **5**, 15422 (2015).

[121] M. V. B. N. L. Balazs and M. V. Berry, "Nonspreading wave packets," Am. J. Phys. **4**, 264–267 (1979).

[122] L. E. Ballentine, Yumin Yang, and J. P. Zibin, "Inadequacy of Ehrenfest's theorem to characterize the classical regime," Phys. Rev. A **50**, 2854 (1994).

[123] G. A. Siviloglou, J. Broky, A. Dogariu, and D. N. Christodoulides, "Observation of accelerating Airy beams," Phys. Rev. Lett. **99**, 213901 (2007).

[124] Georgios A. Siviloglou and Demetrios N. Christodoulides, "Accelerating finite energy Airy beams," Opt. Lett. **32**, 979–981 (2007).

[125] Ido Kaminer, Rivka Benenstein, Jonathan Nemirovsky, and Mordechai Segev, "Nondiffracting accelerating wave packets of Maxwell's equations," Phys. Rev. Lett. **108**, 163901 (2012).

[126] Argha Mondal, Yevick, Aaron, Lauren C. Blackburn, Nikitas Kanellakopoulos, and David G. Grier, "Projecting non-diffracting waves with intermediate-plane holography," Opt. Express **26**, 3926–3931 (2018).

[127] L. Allen, M. W. Beijersbergen, R. J. C. Spreeuw, and J. P. Woerdman, "Orbital angular-momentum of light and the transformation of Laguerre-Gaussian laser modes," Phys. Rev. A **45**, 8185–8189 (1992).

[128] L. Allen, M. J. Padgett, and M. Babiker, "The orbital angular momentum of light," Prog. Opt. **39**, 291–372 (1999).

[129] Jonathan Leach, Miles J. Padgett, Stephen M. Barnett, Sonja Franke-Arnold, and Johannes Courtial, "Measuring the orbital angular momentum of a single photon," Phys. Rev. Lett. **88**, 257901 (2002).

[130] P. Schattschneider, Th. Schachinger, M. Stöger-Pollach, S. Löffler, A. Steiger-

Thirsfeld, K. Y. Bliokh, and Franco Nori, “Imaging the dynamics of free-electron Landau states,” Nat. Comm. **5**, 1–6 (2014).

[131] Christian Schulze, Filippus S. Roux, Angela Dudley, Ronald Rop, Michael Duparré, and Andrew Forbes, “Accelerated rotation with orbital angular momentum modes,” Phys. Rev. A **91**, 043821 (2015).

[132] Peng Zhang, Yi Hu, Tongcang Li, Drake Cannan, Xiobo Yin, Roberto Morandotti, Zhigang Chen, and Xiang Zhang, “Nonparaxial Matthieu and Weber accelerating beams,” Phys. Rev. Lett. **109**, 193901 (2012).

[133] Miguel A. Bandres, Miguel A. Alonso, Ido Kaminer, and Mordechai Segev, “Three-dimensional accelerating electromagnetic waves,” Opt. Express **21**, 13917–13929 (2013).

[134] Ioannis D. Chremmos and Nikolaos K. Efremidis, “Nonparaxial accelerating Bessel-like beams,” Phys. Rev. A **88**, 063816 (2013).

[135] Qian Zhao, Lei Gong, and Yin-Mei Li, “Shaping diffraction-free Lommel beams with digital binary amplitude masks,” Appl. Opt. **54**, 7553–7558 (2015).